Hypersonic and dielectric studies of disordered single crystals, Rb1-x(ND4)xD2Aso4, Na1/2Bi1/2TiO3 and PbMg1/3Nb2/3O3, by brillouin scattering and dielectric measurements
by Chi-Shun Tu

A thesis submitted in partial fulfillment of the requirements for the degree of Doctor of Philosophy in Physics
Montana State University

Abstract:
Temperature and frequency dependent measurements of dielectric permittivity, acoustic sound velocity and damping have been carried out by using Brillouin light scattering and a capacitance and conductance component analyzer on two different types of ferroelectrics, i.e. (i) FE-AFE mixed deuteron glasses Rbl-x(ND4)xD2AsO4 (x=0, 0.10, 0.28), (ii) relaxor ferroelectrics Na1/2Bi1/2TiO3 (NBT) and PbMg1/3Nb2/3O3 (PMN).

In this study, three important results have been observed: (1)A broad and high-value maximum in dielectric permittivity has been observed in relaxors NBT and PMN, which indicates that these materials could be used for electrostrictive displacement transducers. (2) In FE-AFE mixed glasses DRADA-x, a η2μ-type quadratic coupling, squared in order parameter and linear in strain, becomes the main coupling contribution as ammonium ND4 concentration x increases from 0 to an intermediate value. The results also confirm the presence of PE/FE phase coexistence in DRADA-0.10. (3) For both FE-AFE mixed glasses and relaxor ferroelectrics, the order parameter(s) fluctuations, which are generated by the local random fields originating from short-range randomly-placed cations, are the main dynamic mechanisms for hypersonic and dielectric anomalies. In DRADA-0.10 and 0.28, these local randomly-placed ions are ND4+ and Rb+ ions. In PMN, those randomly-placed cations are Mg+2 and Nb+5 which are randomly placed at B-site positions. In NBT, those randomly-placed cations are Na+1 and Bi+3 which are placed randomly at A-site positions.

Two models, i.e. superparaelectric cluster and extrinsic bulk conductivity, also have been proposed to explain the high-temperature and low-frequency dielectric anomaly in NBT. The elastic stiffness and compliance constants are also calculated for PMN.

HYPERSONIC AND DIELECTRIC STUDIES OF DISORDERED SINGLE CRYSTALS, $Rb_{1-x}(ND_4)_xD_2AsO_4$, $Na_{1/2}Bi_{1/2}TiO_3$ AND $PbMg_{1/3}Nb_{2/3}O_3$, BY BRILLOUIN SCATTERING AND DIELECTRIC MEASUREMENTS

by

Chi-Shun Tu

A thesis submitted in partial fulfillment
of the requirements for the degree

of

Doctor of Philosophy

in

Physics

MONTANA STATE UNIVERSITY
Bozeman, Montana

September, 1994

APPROVAL

of a thesis submitted by

Chi-Shun Tu

This thesis has been read by each member of the thesis committee and has been found to be satisfactory regarding content, English usage, format, citations, bibliographic style, and consistency, and is ready for submission to the college of Graduate Studies.

Oct. 3, 1994
Date

V. Hugo Schmidt
Chairperson, Graduate Committee

Approved for the Major Department

10-3-94
Date

Head, Major Department

Approved for the College of Graduate Studies

10/30/94
Date

Graduate Dean

STATEMENT OF PERMISSION TO USE

In presenting this thesis in partial fulfillment of the requirements for a doctoral degree at Montana State University, I agree that the Library shall make it available to borrowers under rules of the Library. I further agree that copying of this thesis is allowable only for scholarly purpose, consistent with "fair use as prescribed in the U.S. Copyright Law". Requests for extensive copying or reproduction of this thesis should be referred to University Microfilms International, 300 North Zeeb Road, Ann Arbor, Michigan 48106, to whom I have granted "the exclusive right to reproduce and distribute my dissertation for sale in and from microform or electronic format, along with the right to reproduce and distribute my abstract in any format in whole or in part."

Signature Chi-Ann Tu

Date Oct. 3, 1994

to my wife Rong-Mei (Ruth), because of whom all things are possible,

and to my son Stachus, in whom I find the reasons

VITA

The author was born Chi-Shun Tu on January 21, 1962 in Kaohsiung, Taiwan. He is the fourth child of Rou-Nu Tu (deceased) and Hsiu-Hsia Tsai Tu and has three older sisters and one younger brother. He was married to Rong-Mei (Ruth) Chien in 1988 and has one son, Stachus Igu Tu.

The author finished his undergraduate work with a B.S in physics at National Taiwan Normal University in 1985. After that time, he was in the Army for two full years to complete his obligation and then taught physics at high school for another two years. From Sept. of 1988 to June of 1990, he attended the University of Oregon in Eugene, Oregon, and graduated with a M.S. in physics. In September of 1990, he enrolled at Montana State University as a graduate teaching and research assistant until the fall of 1994, obtaining a Ph.D. in physics under Professor V. Hugo Schmidt.

ACKNOWLEDGMENTS

I would like to sincerely thank my advisor Prof. V. Hugo Schmidt for his support, advice, and encouragement over the past four years. Whenever I became confused or frustrated by the experiments, he was there with the appropriate advice and help. Dr. Igor G. Siny and Greg Pastalan helped me to set up the experimental system and taught me Brillouin scattering skills. I give Igor and Greg my appreciation for sharing their ideas with me and for so much technical guidance that was given freely.

Thanks to Prof. G.F. Tuthill for endless theoretical teaching and discussion, to Bob Parker for his technical support on computer software and hardware issues, to Dr. Toby Howell who helped me to learn dielectric measurements, and to Norm Williams and Erik Anderson for their technical help and friendship.

My wife Rong-Mei (Ruth) deserves my deepest appreciation for her constant support, encouragement and sacrifices. Stachus my son I rely upon to always bring a smile to my face and my heart.

My appreciation also goes to the National Science Foundation for the support I received under grant number DMR-9017429.

Finally, I would like to thank my parents, especially my mother. She gave us much help during the first six months since Stachus was born and during writing the thesis. They may not understand what I am doing, but they understand me. Their encouragement and support played an important role in the completion of this thesis.

TABLE OF CONTENTS

TABLE OF CONTENTS–CONTINUED

LIST OF TABLES

LIST OF FIGURES

LIST OF FIGURES–CONTINUED

LIST OF FIGURES–CONTINUED

LIST OF FIGURES–CONTINUED

LIST OF FIGURES–CONTINUED

LIST OF FIGURES–CONTINUED

Figure Page

LIST OF FIGURES–CONTINUED

ABSTRACT

Temperature and frequency dependent measurements of dielectric permittivity, acoustic sound velocity and damping have been carried out by using Brillouin light scattering and a capacitance and conductance component analyzer on two different types of ferroelectrics, i.e. (i) FE-AFE mixed deuteron glasses $Rb_{1-x}(ND_4)_xD_2AsO_4$ (x=0, 0.10, 0.28), (ii) relaxor ferroelectrics $Na_{1/2}Bi_{1/2}TiO_3$ (NBT) and $PbMg_{1/3}Nb_{2/3}O_3$ (PMN).

In this study, three important results have been observed: (1) A broad and high-value maximum in dielectric permittivity has been observed in relaxors NBT and PMN, which indicates that these materials could be used for electrostrictive displacement transducers. (2) In FE-AFE mixed glasses DRADA-x, a $\eta^2\mu$-type quadratic coupling, squared in order parameter and linear in strain, becomes the main coupling contribution as ammonium ND_4 concentration x increases from 0 to an intermediate value. The results also confirm the presence of PE/FE phase coexistence in DRADA-0.10. (3) For both FE-AFE mixed glasses and relaxor ferroelectrics, the order parameter(s) fluctuations, which are generated by the local random fields originating from short-range randomly-placed cations, are the main dynamic mechanisms for hypersonic and dielectric anomalies. In DRADA-0.10 and 0.28, these local randomly-placed ions are ND_4^+ and Rb^+ ions. In PMN, those randomly-placed cations are Mg^{+2} and Nb^{+5} which are randomly placed at B-site positions. In NBT, those randomly-placed cations are Na^{+1} and Bi^{+3} which are placed randomly at A-site positions.

Two models, i.e. superparaelectric cluster and extrinsic bulk conductivity, also have been proposed to explain the high-temperature and low-frequency dielectric anomaly in NBT. The elastic stiffness and compliance constants are also calculated for PMN.

CHAPTER 1

INTRODUCTION

Introduction to Disordered Crystals

If the composition in a crystal is not completely uniform (compositional heterogeneity) down to the unit cell scale or has cation fluctuations statistically or dynamically, then the crystal is usually called "disordered".[1] In terms of symmetry, "disordered" means that there is no long-range translational symmetry inside the crystal. Among disordered materials, many experiments have concentrated on two different systems, i.e. ferroelectric (FE)-antiferroelectric (AFE) mixed crystals with the general formula $A_{1-x}(NH_4)_xH_2BO_4$ [A=Rb, K, Cs and Tl, B=P and As][2-11] and complex relaxor ferroelectrics with formula $(A'_xA''_{1-x})^{+2}B^{+4}O_3^{-2}$ or $A^{+2}(B'_xB''_{1-x})^{+4}O_3^{-2}$.[1,12,13] In these systems, local random fields originating from randomly-placed cations (or ions) play an important role for physical properties such as acoustic (sound velocity and damping) and dielectric anomalies. Since local random fields can suppress the long-range electric ordering and produce the order parameter fluctuations, a normal sharp phase transition usually is not observed in these materials. "Diffuse" (non-sharp peak) phase transition is the typical anomalous characteristic of these disordered materials. The two-dimensional distributions of ions (or cations) for both ordered and disordered states are given schematically in Fig. 1.

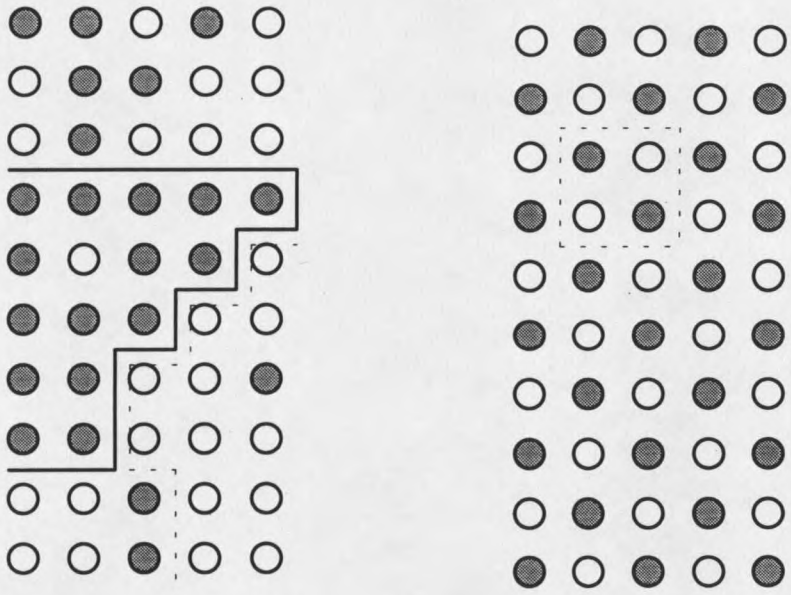

(a) (b)

$(A_1A_2)BO_3$, $A(B_1B_2)O_3$, $A_x(NH_4)_{1-x}H_2BO_4$ and $A_x(ND_4)_{1-x}D_2BO_4$

Disordered State	Ordered State
—A_1(●), B_1(●) or A(●) rich region	Uniform composition
····A_2(O), B_2(O) or $NH(D)_4$(O) rich region	Full translational symmetry

Figure 1. Two-dimensional illustrations of ordered and disordered states for both FE-AFE mixed glasses $A_x(NH_4)_{1-x}H_2BO_4$ [or $A_x(ND_4)_{1-x}D_2BO_4$] and complex relaxor ferroelectric systems $(A_1A_2)BO_3$, $A(B_1B_2)O_3$.

For relaxor ferroelectrics, one can use thermal treatments such as annealing, quenching and ratio of cations to control ordering.[1] In FE-AFE mixed proton glasses, the crystal ordering depends on ammonium concentration.[2-7] From experimental results, some general differences have been found between ordered and disordered ferroelectrics:

(1) Ordered (normal):

a) Sharp dielectric phase transition at T_c

b) Stable remanent polarization

c) No strong dielectric frequency dependence at phase transition

d) Stable birefringence

e) No local random fields

f) Usually no intermediate phase between high- and low-symmetries

(2) Disordered:

a) Diffuse dielectric transition which doesn't correspond to any specific change of symmetry (or phase)

b) No stable remanent polarization

c) Strong frequency dependence at diffuse transition

d) No stable birefringence

e) Strong local random fields

f) Usually associated with a sequence of phase transitions, i.e. one (or more) intermediate phase occurred between high- and low-symmetries

In this study, five different single crystals have been measured, i.e. FE-AFE mixed deuteron glasses, $Rb_x(ND_4)_{1-x}D_2AsO_4$ with x=0, 0.10 and 0.28 and complex relaxor ferroelectrics, $Pb(Mg_{1/3}Nb_{2/3})O_3$ (PMN) and $Na_{1/2}Bi_{1/2}TiO_3$ (NBT). The introductions to these two different systems are given below.

Relaxor Ferroelectrics (RF)

Perovskite is the name of the mineral calcium titanate ($CaTiO_3$). Most of the useful piezoelectric (ferroelectric) crystals, such as barium titanate ($BaTiO_3$), lead titanate ($PbTiO_3$), lead zirconate titanate ($PbZr_{1-x}Ti_xO_3$), lead lanthanum zirconate titanate (PLZT), sodium bismuth titanate $Na_{1/2}Bi_{1/2}TiO_3$ and lead magnesium niobate $Pb(Mg_{1/3}Nb_{2/3})O_3$ etc., have perovskite-type structure, i.e. ABO_3-type unit cell.[13] Here "O" is oxygen, "A" represents a cation with a larger ionic radius, and "B" a cation with a

smaller ionic radius. Fig. 2 shows a typical cubic ABO_3 perovskite-type structure in the paraelectric phase and possible directions of distortion in the ferroelectric phase.[14]

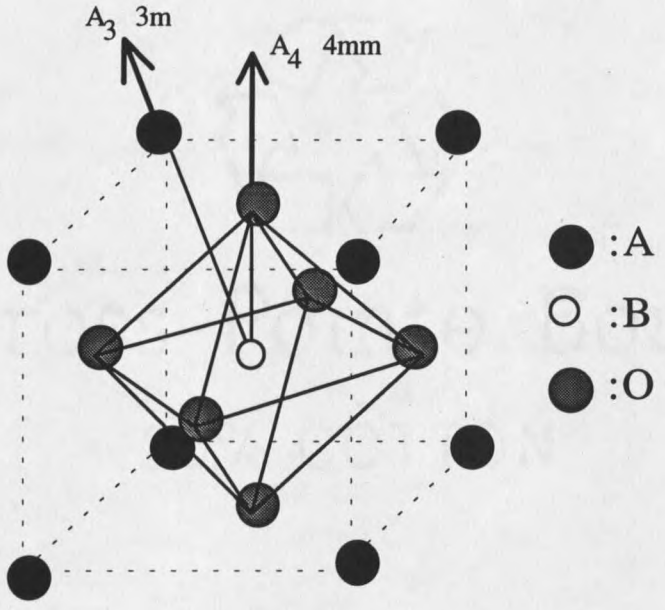

Figure 2. A perovskite cubic unit cell. The point group usually is m3m for a paraelectric cubic ABO_3 perovskite-type structure. Solid lines indicate the BO_6 octahedron. A_4 indicates one of three 4-fold rotation axes and 4mm is the usual corresponding point group in the tetragonal ferroelectric phase. A_3 indicates one of four 3-fold rotation axes and 3m is the usual corresponding point group in the trigonal ferroelectric phase.

Many of the complex relaxor ferroelectrics with perovskite-type structure are compounds with either $A^{+2}B^{+4}O_3^{-2}$ or $A^{+1}B^{+5}O_3^{-2}$-type formula. In the perovskite family, there are many compounds with the formula $A^{+3}B^{+3}O_3^{-2}$, but among them no ferroelectrics have been discovered.[13]

The perovskite structure is essentially a three-dimensional network of BO_6 octahedra (see Fig. 2). It may also be regarded as a cubic close-packed arrangement of A and B ions with B ions filling the octahedral interstitial positions.[13] The packing situation of this structure may be characterized by a tolerance factor t, which is defined by the following equations:[13]

$$R_A + R_O = t\sqrt{2}(R_B + R_O) \quad (1)$$

or

$$t = \frac{R_A + R_O}{\sqrt{2}(R_B + R_O)} \quad (2)$$

where R_A, R_B and R_o are the ionic radii of A, B and O ions, respectively. When t is equal to 1, the packing is said to be ideal. When t is larger than 1, there is too large a space available for the B ion, and therefore this ion can "move" inside its octahedron. In general, to form a stable perovskite structure, one requires that $0.9<t<1.1$. Besides the ionic radii, other factors, such as polarizability and character of bonds, must also be taken into account.[13]

The term "complex relaxor ferroelectrics" generally refers to the complex perovskites in which the charge classifications of $(A'_xA''_{1-x})^{+2}B^{+4}O_3^{-2}$ or $A^{+2}(B'_xB''_{1-x})^{+4}O_3^{-2}$ etc. are satisfied and unlike-valence cations belonging to a given site (A or B) are present in the correct ratio for charge balance, but are situated randomly on these cation sites. For example, sodium bismuth titanate $Na_{1/2}Bi_{1/2}TiO_3$ has two unlike valence cations Na^+ and Bi^{+3} distributed in the A site and lead magnesium niobate $Pb(Mg_{1/3}Nb_{2/3})O_3$ has two unlike valence cations Mg^{+2} and Nb^{+5} distributed in the B site.[1,15,16] These randomly different cation charges give rise to random electric fields and cause random elastic distortion fields in microregions. These random fields tend to make the phase transitions "diffuse" instead of sharp as in normal ferroelectrics, and complicate the task of determining structure and state of electric order. The electric properties of relaxor ferroelectrics also depends on the cation ordering degree. The degree of ordering inside a crystal depend on several things such as method of crystal growth, cation valence, and thermal treatment (e.g. quenching and annealing). In certain compounds,

such as $PbSc_{1/2}Ta_{1/2}O_3$ (PST) and $PbIn_{1/2}Nb_{1/2}O_3$ (PIN), the driving force for cation ordering is such that long-range coherence and corresponding normal FE (or AFE) behavior can be achieved through thermal annealing.[15] An additional complication is the aging effect which can span a wide time scale in a nonlinear manner. Relaxor ferroelectrics usually exhibit a sequence of anomalies in the dielectric response as temperature changes.[1,16] However, the dielectric maximum does not clearly mark a phase transition into a low-symmetry region.

It is important to note that B-site order in $A^{+2}(B'_xB''_{1-x})^{+4}O_3^{-2}$ compounds could be either stoichiometric (ordered) or nonstoichiometric (disordered) as shown in Fig. 3.[1,15]

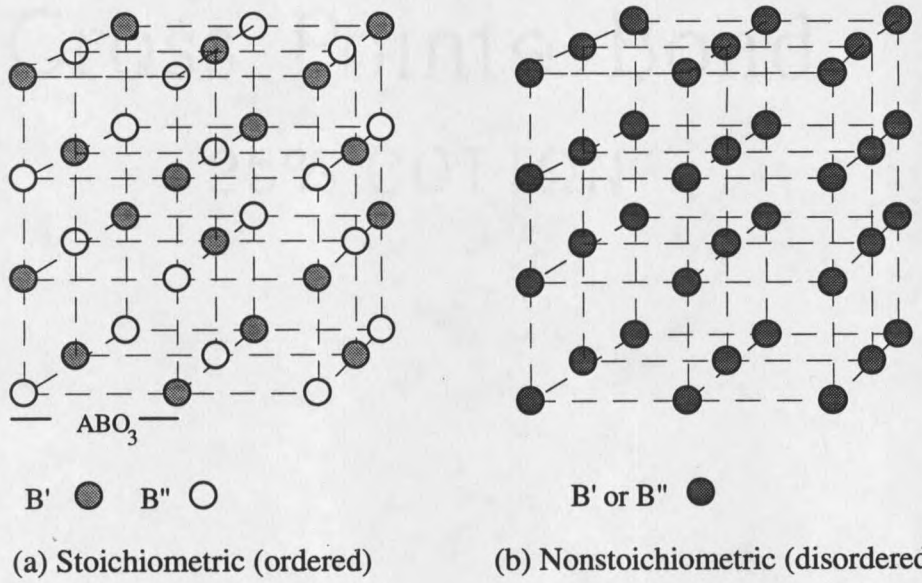

(a) Stoichiometric (ordered) (b) Nonstoichiometric (disordered)

Figure 3. Mixed-ion arrangements of (a) ordered and (b) disordered cubic perovskite ABO_3 structure.

For example, B-site order in x=1/2 compounds, e.g. $Pb(Sc_{1/2}Ta_{1/2})O_3$ and $Pb(Mg_{1/2}W_{1/2})O_3$, results in an average valence of +4 and thus is referred to as stoichiometric ordering.[15] In contrast, nonstoichiometric ordering is found in x=1/3 compounds, e.g. $Pb(Mg_{1/3}Nb_{2/3})O_3$ and $Pb(Cd_{1/3}Nb_{2/3})O_3$ where a tendency toward 1:1

B'B" order is observed and as such the average charge value is lower than the expected valence of +4. The overall defect chemistry and average compensation mechanism of the nonstoichiometric ordering are not well understood at this time.

A sequence of phase transitions with one or two intermediate phase is a characteristic of complex relaxor ferroelectrics.[1,16] A general schematic phase diagram is given in Fig. 4.

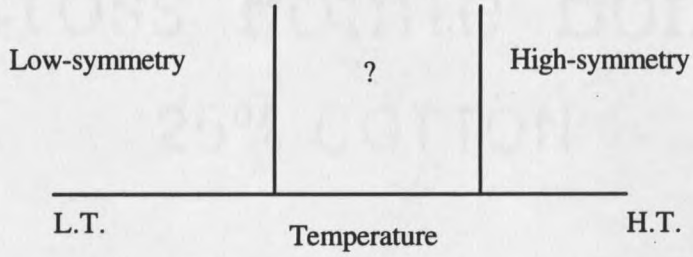

Figure 4. A general schematic phase diagram vs. temperature for complex relaxor ferroelectrics. "?" indicates one or two intermediate regions.

Proton (or Deuteron) Glasses (PG)

At room temperature, the hydrogen-bonded phosphates (MH_2PO_4) and arsenates (MH_2AsO_4) (M=Na, K, Rb, Cs, Ag, Tl and NH_4) form a class of KDP-type isostructural crystals of tetragonal symmetry.[17] The structure of KH_2PO_4 (KDP) at room temperature is given in Fig. 5.[17]

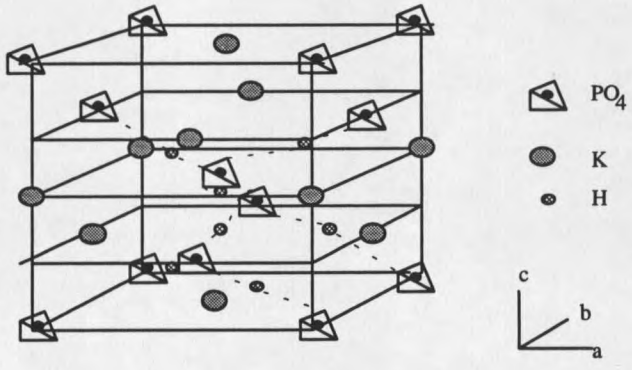

Figure 5. The structure of KDP at room temperature. Here just a few hydrogen bonds are shown.

When M is an alkali ion, the low-temperature state is ferroelectric. However, it should be noted that RDP can be grown in either a tetragonal or a monoclinic structure. Fig. 6 is the c-axis projection of KDP structure in the ferroelectric phase ($T<T_c$).[17]

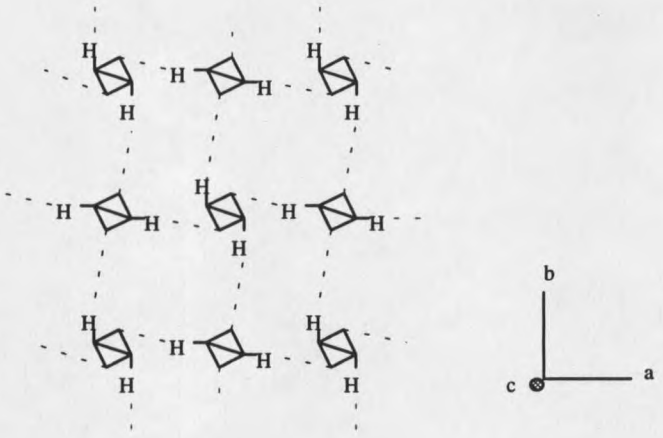

Figure 6. Projection of KDP along c-axis in the ferroelectric phase ($T<T_c$). The solid line inside the square connects oxygen atoms at the same height.

The KDP-type structure consists of two interpenetrating sublattices. One is a body-centered sublattice of PO_4 tetrahedra and the other is a body-centered sublattice of K^+ ions. The hydrogen atoms are dynamically fluctuating between off-center positions but are statistically distributed at the centers of the O···H···O bonds in the paraelectric (PE) phase. They are in ordered off-center positions in the ferroelectric (FE) phase. In the FE phase the protons are either close to the "upper oxygens" or "lower oxygens" and the non-zero net polarization depending on domain type arises from the displacement of K^+ and P^{5+} ions along the c-axis direction.

The ammonium compounds which exhibit a paraelectric (PE)-antiferroelectric (AFE) phase transition have NH_4^+ substituted for K^+ position in the KDP-type unit cell. Two of the four "ammonium" protons form short bonds with the surrounding PO_4 tetrahedra as seen in Fig. 7.

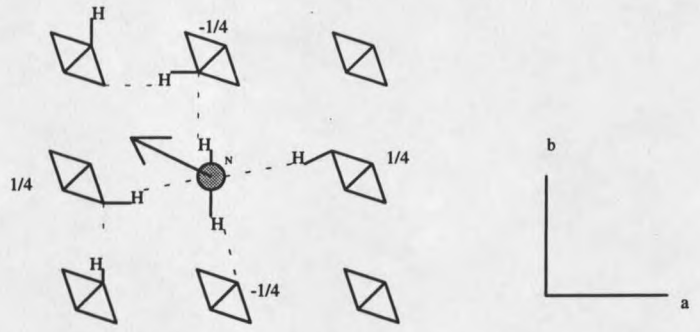

Figure 7. The structure of ADP projected along the c-axis. A NH_4^+ at height 0 is shown attached to nearby oxygens of PO_4 tetrahedra. The heights in unit of c of the phosphorus centers of the PO_4 tetrahedral are indicated. The PO_4 tetrahedron located above the ammonium, at height 1/2, and a number of protons, are not shown. The off-center motion of the ammonium ion is indicated by the arrow. This is one of the four possible directions of this arrow in the (001) plane.

In the antiferroelectric phase the positions of the "acid" protons are such that each PO_4 tetrahedron has one close proton each at the upper and the lower sides, unlike in KDP where in the FE phase all the "acid" protons are attached either to the top or bottom of the PO_4 tetrahedron. Such an arrangement of the "acid" protons results in local dipoles alternately pointing "up" and "down" along the a-axis (or b-axis) direction as shown in Fig. 8, and yielding zero net polarization.

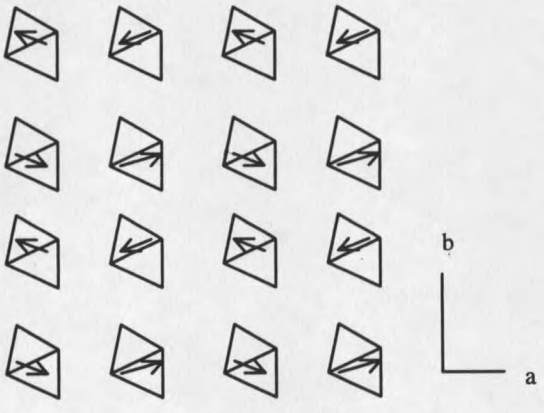

Figure 8. Schematic representation of the antiferroelectric phase of ADP (or ADA)

It is important to note that the deuterated isomorphs show enhanced electric-ordering temperatures (isotope effect).[17] For instance, T_c is 146 K for RbH_2PO_4 and T_c is 218 K for RbD_2PO_4. Such isotope effects occur not only for pure ferroelectrics but also for FE-AFE mixed crystals.[2]

The FE-AFE mixed crystals $A_{1-x}(NH_4)_xH_2BO_4$ and $A_{1-x}(ND_4)_xD_2BO_4$ usually exhibit a frequency dependent dielectric anomaly instead of a phase transition for certain intermediate values of x. In these systems, competition between the FE and the AFE orderings which are characterized by specific configurations of the acid protons, plays an important role for dynamic anomalies. The random distribution of the Rb (or K, Cs, Tl) and NH_4 (or ND_4) cations is the origin of the local random fields. At lower temperature the system eventually becomes nonergodic in which case the system is frozen completely on a practical time scale.[8] This behavior is reminiscent of that of magnetic spin glasses, except that the random bias field caused by random Rb and NH_4 neighbor placement biasing the O-H···O bonds smears out the spin glass "transition". However, whether there is a real ergodic-nonergodic transition is still an open question. From the experimental results, it was found that small amounts of ammonium admixtures are sufficient to stabilize the tetragonal structure even at low temperature. A typical schematic phase diagram of proton (or deuteron) glass is shown in Fig. 9.[7,18]

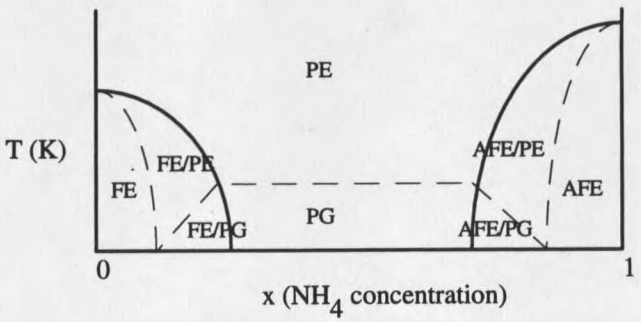

Figure 9. Schematic phase diagram of FE-AFE mixed glasses such as RADP. PG: proton glass, PE/FE: PE and FE phase coexistence region.

Previous Knowledge for Crystals Discussed in This Thesis

$Na_{1/2}Bi_{1/2}TiO_3$ (NBT)

$Na_{1/2}Bi_{1/2}TiO_3$ undergoes a cubic-tetragonal-trigonal succession of structural phase transitions, ending in a ferroelectric state at room temperature. Different studies on NBT have been published in many papers,[19-30] but its behavior is still far from clear. Most of the contradictions concern the number and location of different phases as well as the electrical state in each phase. According to x-ray[23] and neutron measurements[30] there are two structural phase transitions in NBT from the high-temperature cubic phase to a tetragonal and then a trigonal phase. The tetragonal phase seems to be ferroelastic as shown by domain pattern visualization.[24] However, the question of whether this phase is polar is still open. Some dielectric measurements indicate that an antiferroelectric phase exists between the tetragonal ferroelastic and trigonal ferroelectric phases. However, x-ray and neutron scattering studies have not provided any evidence to support this view. Neutron scattering indicates that the transition between tetragonal and trigonal phases is characterized by a region of phase coexistence. However, the nature of the high-frequency dielectric maximum near 640 K is still an open question.[16]

$Pb(Mg_{1/3}Nb_{2/3})O_3$ (PMN)

Dielectric results of PMN shows a frequency dependent "diffuse" phase transition associated with a broad maximum around 270 K.[1] This anomaly is attributed to quenched random electric fields originating from charged compositional fluctuations.[31] Under a strong bias electric field (≥4 kV/cm), an additional dielectric peak occurs at T_c~ 210 K below which the random fields are overcome by the external electric field.[31]

In the supposedly disordered PMN single crystal, a microstructure on a nanometric length scale with 1:1 cation ordering in B site was reported.[32,33] Such 1:1 ordering, when charge neutrality requires 1:2 stoichiometry, implies locally charged

regions causing fields which induce random polarization. Recent results show only a 5% tendency toward 1:1 ordering in these microregions.[34]

Three recent models for the relaxor ferroelectric crystal PMN have been proposed, namely the random field model (RF),[31] the dipolar glass model[35] and the structural model.[36] The first two models are based on the temperature and electric field responses of these microdomains. The last model, based on x-ray and neutron powder diffraction at 5 K, indicates an average cubic structure even at 5 K, but with some 20% of the material in non-cubic FE microdomains near 100 Å size.

The RF model postulates random electric fields originating in a peculiarity of PMN's structure, i.e. local nonstoichiometric order causing local net charge, resulting in microdomains polarized along the 8 <111> directions, and assumes that the cubic anisotropy corresponding to these 8 directions is low enough so that the random fields can suppress the FE transition.

In the dipolar glass model for PMN, the "pseudospins" are nanometer-sized superparaelectric clusters which correspond to the microdomains in the random fields model. This model assumes that these superparaelectric clusters can flip at higher temperature, but freeze into a random configuration at lower temperature. However, the random field model seems to imply that microdomains have fixed orientations determined by local fields.

Recent results of the linear birefringence $\Delta n \propto \langle P_{//}^2 \rangle - \langle P_{\perp}^2 \rangle$ in PMN under an external electric field suggest an equilibrium phase transition temperature T_c in the absence of the random fields, $200\ K < T_c < 234\ K$.[31] In addition, by fitting the time dependence of the linear birefringence with two different exponents β below and above 212 K, Westphal *et al.* propose that the Curie temperature of PMN is $T_c \sim 212$ K. Viehland *et al.* also claim that the freezing temperature is $T_f \sim 217$ K in PMN below which a dramatic change of the relaxation time distribution is observed and is interpreted as a

result of a long-range correlation of polar microdomains.[31] Recent quasielastic-neutron scattering (QES) on PMN supports the above interpretations and shows that the correlation length is nearly temperature independent with a maximum value of 200 Å below ~217 K.[35]

$Rb_{1-x}(ND_4)_xD_2AsO_4$ (DRADA-x=0, 0.10, and 0.28)

Pure DRDA (x=0) single crystal exhibits a first-order PE↔FE phase transition at T_c~165 K as observed from spontaneous polarization measurement. The ND_4^+ deuteron NMR spectra of DRADA-0.10 showed a gradual disappearance of the doublet near 131 K where the single broad linewidth grows to its full size,[37] from which it is concluded that below 131 K the FE phase portion is greater than PE in the crystal and becomes the dominant ordering. This result is consistent with the presence of PE/FE phase coexistence as evidenced by dielectric results which show that a gradual ferroelectric transition begins at T_m=146 K and is mostly completed at ~120 K.[7] The remaining PE material begins exhibiting dielectric dispersion characteristic of deuteron glass below a frequency-dependent temperature T_g, which is 60 K at 50 kHz. DRADA–0.28 has only a frequency dependent dielectric anomaly separating PE from deuteron glass behavior at T_g~65 K (f=0.1 MHz). Field-heated, field-cooled and zero-field-heated static permittivity revealed that below T_e~38 K (nonergodic temperature) the system enters a nonergodic state in which for practical purposes the acid deuteron of the O-D···O bond is frozen completely.[8]

Purpose and Outline of The Present Work

Both piezoelectric (strain linearly proportional to applied electric field) and electrostrictive (strain proportional to square of applied electric field) effects are important phenomena in ferroelectrics.[13] These two intrinsic electric responses have

been used for applications in many ways such as nanometer-scale actuators and sensors. The main advantages of electrostrictive actuators include insignificant hysteresis and less creep and susceptibility aging (gradual change in response with time) which are the problems of piezoelectric actuators (or sensors). Brillouin light scattering and dielectric methods are powerful tools to understand both piezoelectric and electrostrictive couplings. The elastic stiffness and piezoelectric stress constant can also be obtained from these measurements. The overall purpose of this study is to provide a basis for improving properties useful in applications and extending the useful temperature range upward and downward in disordered ferroelectrics.

In this study, FE-AFE mixed glasses $Rb_{1-x}(ND_4)_xD_2AsO_4$ (x=0, 0.10, and 0.28) and complex perovskites $Na_{1/2}Bi_{1/2}TiO_3$ and $Pb(Mg_{1/3}Nb_{2/3})O_3$ have been measured by two different methods, i.e. Brillouin light scattering (θ_s=180°, 32.6° and 12.6°) and dielectric permittivity ($\varepsilon^*=\varepsilon'-i\varepsilon''$) between 0.02 and 300 kHz. The experimental procedure will be discussed in chapter 2.

CHAPTER 2

EXPERIMENTAL PROCEDURES

Crystal Growth and Sample Preparation

Single crystals of $Rb_{1-x}(ND_4)_xD_2AsO_4$, (x=0, 0.10, 0.28) for Brillouin scattering and dielectric permittivity measurements were grown here from aqueous solutions with certain ratios of RbD_2AsO_4 (DRDA) and $(ND_4)D_2AsO_4$ (DADA) at room temperature. These starting materials were grown by following chemical reactions:

$$Rb_2CO_3 + As_2O_5 + D_2O \Rightarrow 2RbD_2AsO_4 + CO_2$$
$$(ND_4)_2CO_3 + As_2O_5 + 2D_2O \Rightarrow 2(ND_4)D_2AsO_4 + CO_2$$

These DRADA crystals were carefully polished to be rectangular with average size of 1.2 $\times 0.4 \times 0.2$ cm^3. A general growth formula for this type of mixed crystals is given below.

KDP-type FE crystals	+	ADP-type AFE crystals	$\Rightarrow$	FE-AFE glasses
$\Downarrow$		$\Downarrow$		$\Downarrow$
$(1-x)\cdot AH_2BO_4$	+	$x\cdot NH_4H_2BO_4$	$\Rightarrow$	$A_{1-x}(NH_4)_xH_2BO_4$
$(1-x)\cdot AD_2BO_4$	+	$x\cdot ND_4D_2BO_4$	$\Rightarrow$	$A_{1-x}(ND_4)_xD_2BO_4$

(Here A=Rb, K, Cs and Tl, B=P and As)

The solvent for deuterated crystals is heavy water. Such a "solution growth" is a two component system, i.e. solute and solvent, and so requires simultaneous control of two parameters (temperature and concentration x) during the crystallization process. The difficulty of crystal growth also depends on whether the cation sizes match each other. For instance, the rubidium and ammonium ions are a nearly perfect match in size, so high-quality and strain-free mixed single crystals of $Rb_{1-x}(NH_4)_xH_2PO_4$ can be grow at all concentrations x.[18]

Relaxor ferroelectric single crystals NBT and PMN were grown by the Czochralski method in A. F. Ioffe Physical Technical Institute, with dimensions 5.57× 6.03×5.74 $(mm)^3$ and 5.37×4.77×2.82 $(mm)^3$, respectively. The Czochralski growing method can be found in Ref. 38. For dielectric measurements, a silver paste (Ted Pella #16032) was used for the electrodes.

Dielectric Permittivity

For the audio frequency range (0.02–300 kHz), a Wayne-Kerr Model 6425 Precision Component Analyzer with 4-lead connections was used for capacitance and conductance measurements. A Leybold RGD-210 closed cycle helium refrigerator was used for low temperatures (10-300 K) with a silicon diode temperature sensor put immediately below the sample holder. For high temperatures (300-900 K), an oven was used with a calibrated LakeShore PT-103 platinum resistance thermometer which was put just above the sample. The temperature accuracy is about ±0.1 K. All data were collected automatically with frequency swept in steps from 0.02 to 300 kHz. The measuring voltage was 0.5 V. The error of the dielectric relative permittivities (ε' and ε'') is about 0.05%.

Brillouin Light Scattering

The light scattering caused by acoustic phonons is called Brillouin scattering, for which the frequency shift $\Delta\nu$ is between 0.01 and 5 cm^{-1}. In Raman scattering, the frequency shift $\Delta\nu$ is usually caused by molecular vibrations or optical phonons and is generally larger than 5 cm^{-1}. The elastic or quasielastic ($\Delta\nu \approx 0$) scattering processes which are caused by inhomogeneous distribution of the refractive index in a crystal are called Rayleigh scattering.

For visible light (usually from a high intensity laser beam), the photon wave vectors (of order 10^5 cm^{-1}), i.e. $\lambda \sim 5000$ Å, are small compared with the Brillouin zone dimension (of order 10^8 cm^{-1}), thus information is provided by Brillouin scattering only about phonons in the immediate neighborhood of $\vec{k}=0$. In order to estimate the order of magnitude of the acoustic phonon cutoff frequency ω_c, a simple dispersion curve $\omega(k)$ of the longitudinal mode from a monatomic linear chain with only nearest-neighbor interaction is considered in Fig. 10.[39]

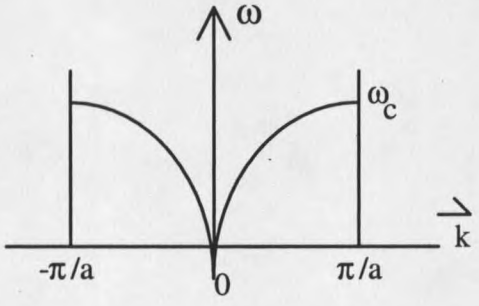

Figure 10. Dispersion curve of $\omega(k)$ of the longitudinal mode from a monatomic linear chain. At any frequency below the cutoff frequency $\omega_c = 2\sqrt{K/M}$, two waves can propagate in both directions with opposite wave numbers.

For a monatomic linear chain lattice, the acoustic phonon frequency is $\omega = 2\sqrt{K/M}|\sin ka/2|$.[39] K is the force constant whose value depends on temperature

and different vibration modes. M is the mass of the atom. For small wave number, i.e. ka<<1, we then have $\omega = ka\sqrt{K/M}$, i.e. $a\sqrt{K/M}=\omega/k=V_o$. V_o is the acoustic phonon velocity near the Brillouin zone center, i.e. $\bar{k}\sim 0$. When the wavelength is of the order of magnitude of the interatomic distance a (ka comparable to π), the frequency of acoustic phonons is bounded by the cutoff frequency, i.e. $f_c = \sqrt{K/M}/\pi = V_o/a\pi$. The V_o in dielectric solids lies between 10^3 and 10^4 m/s. The interatomic distance is a few Å. Taking $V_o=5\times10^3$ m/s and a=5 Å, the cutoff frequency is $f_c=3.2\times10^{12}$ GHz.

Brillouin light scattering can provide three types of basic information; (i) acoustic phonon frequency shift (sound velocity) from which the elastic and piezoelectric constants can be obtained, (ii) half-width at half height (damping or life time of phonon) and (iii) intensity of background which usually is related to the central component.

General Description of Experiment

The Brillouin spectra were obtained from several different scattering angles which include backscattering ($\theta_s=180^o$) and small angles ($\theta_s=12.6^o$, 32.6^o). Scattering angle means the angle between incident and scattered wave vectors inside the crystal. An actual determination of scattering angle is given in Fig. 11.

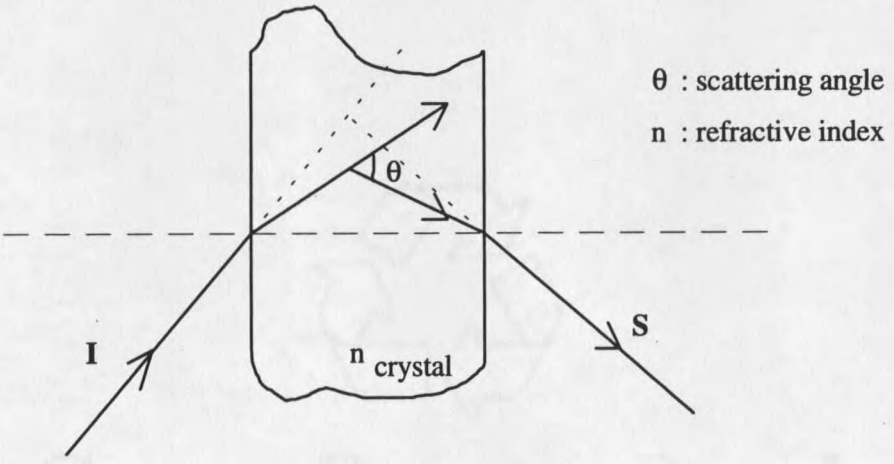

Figure 11. The determination of the Brillouin scattering angle θ.

The scattering geometry is usually expressed by a notation such as Z(X,Y)X for light scattering by a crystal. The notation stands for $\vec{K}_I(\vec{E}_I,\vec{E}_S)\vec{K}_S$ where $\vec{E}_I$ and $\vec{E}_S$ are polarization vectors of the incident ($\vec{I}$) and scattered ($\vec{S}$) beams, respectively. The first and last letters of Z(X,Y)X indicate that the propagation directions of the incident and scattered beams are parallel to the Z and X axes, respectively. The two letters in parentheses indicate that the polarization directions of the incident and scattered beams are parallel to the X and Y axes, respectively. Therefore, Z(X,Y)X corresponds to the experimental set-up illustrated in Fig. 12a. In case of isotropic materials (or in case the detailed specification of the scattering geometry is unnecessary or difficult), the geometry is expressed by two letters such as HV. "HV" means that $\vec{E}_I$ is parallel to the plane and $\vec{E}_S$ is perpendicular to the plane, as illustrated in Fig. 12b. The plane is determined by $\vec{K}_I$ and $\vec{K}_S$.

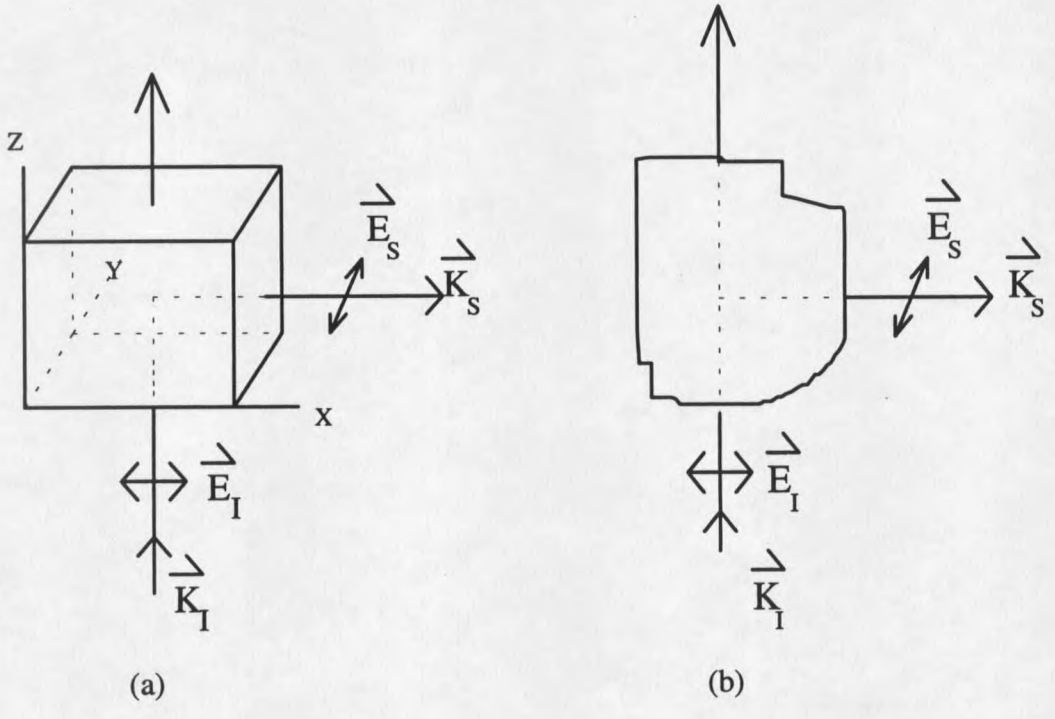

Figure 12. Symbols of scattering geometries. (a) Z(X,Y)X, (b)HV.

In order to reduce the low-lying frequency mode of the Raman spectra, a narrow-band (1 Å) interference filter was used. All samples were illuminated by a Lexel Model 95-2 argon laser with λ=514.5 nm. Scattered light was analyzed by a Burleigh five-pass Fabry-Perot interferometer. The laser line broadening due to the jittering was claimed by the manufacturer to be about 10 MHz (half-width).

For small angle (θ_s<180°) Brillouin scattering, the experimental set-up is shown in Fig. 13. The lens L_1 serves to focus the incident beam into the sample which was set in the closed-cycle cryostat. The distance between L_2 and the sample is the focus length of lens L_2. The scattered beam from the sample is collected by L_2 and then becomes parallel. The lens L_3 focuses the parallel scattered light at the center of a 200 μm-radius pinhole, and the transmitted light is collimated by the lens L_3. The collimated beam passes a narrow-band (1 Å) interference filter and then enters a Burleigh five-pass Fabry-Perot interferometer. The light from the Fabry-Perot interferometer is focused at the end of the telemeter with a 200 μm pinhole.

A Model R464 head-on photomultiplier (PMT) was used to collect the transmitted light from the telemeter. A home-made high voltage power supply provides a maximum voltage of 1450 V for the cathode of the PMT. A home-made voltage amplifier was used to amplify the analog output from the PMT. The analog output from the amplifier was fed into a home-made analog→TTL transformer and then connected with a Dell 486 computer through a Computer Boards Inc. Model CIO-AD08 (8-channel) AD/DA converter. The Brillouin spectrum was displayed on the screen and stored as an ASCII file. A shutter was used to reduce the Rayleigh line intensity. If the intensity of the Rayleigh line exceeds a certain value which was determined beforehand, the shutter is closed during the Rayleigh spectrum range. After a certain closing time which was also programmed preliminarily, it will be opened during the Brillouin spectrum range.

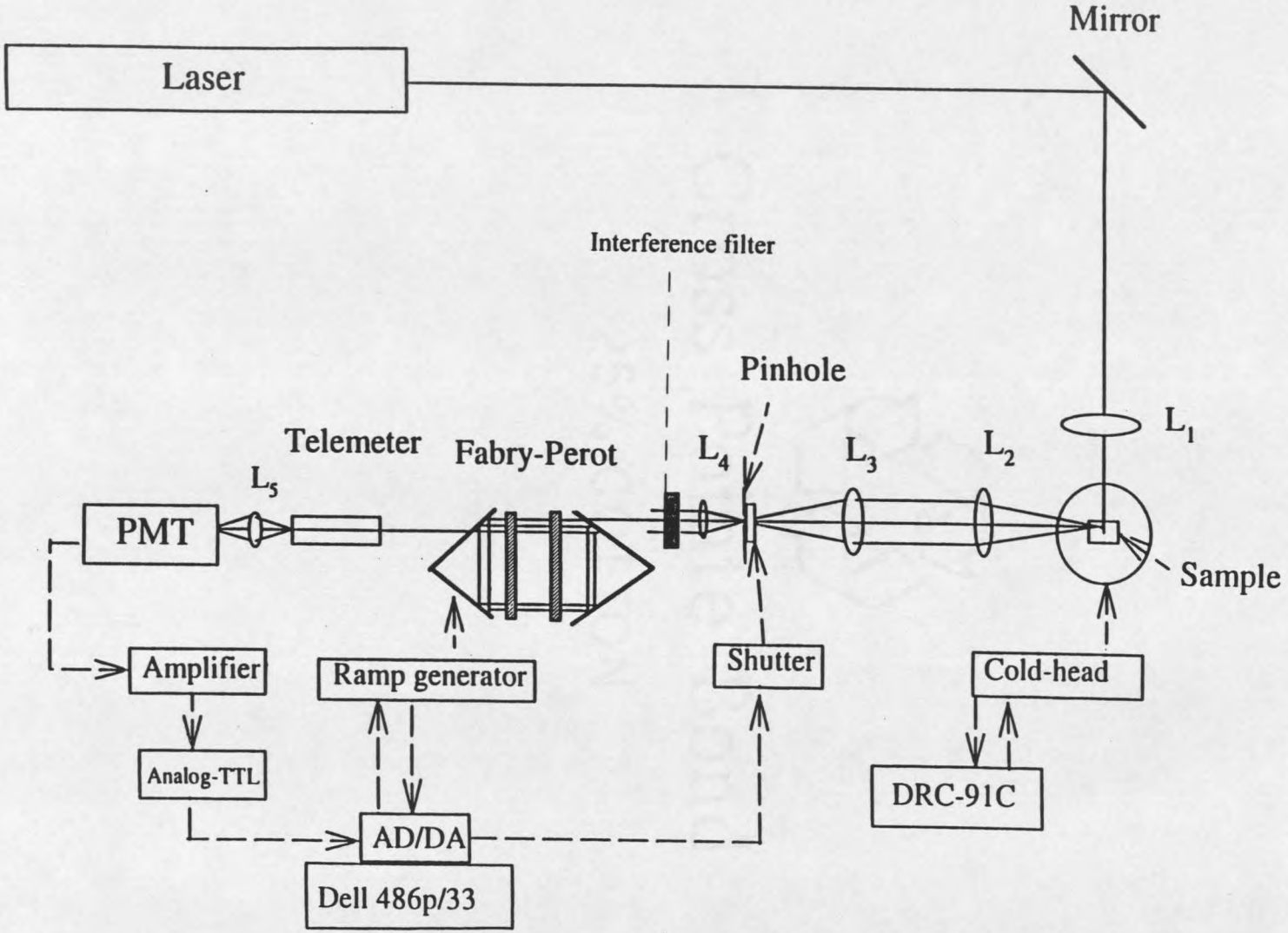

Figure 13 Brillouin scattering set-up for small angles.

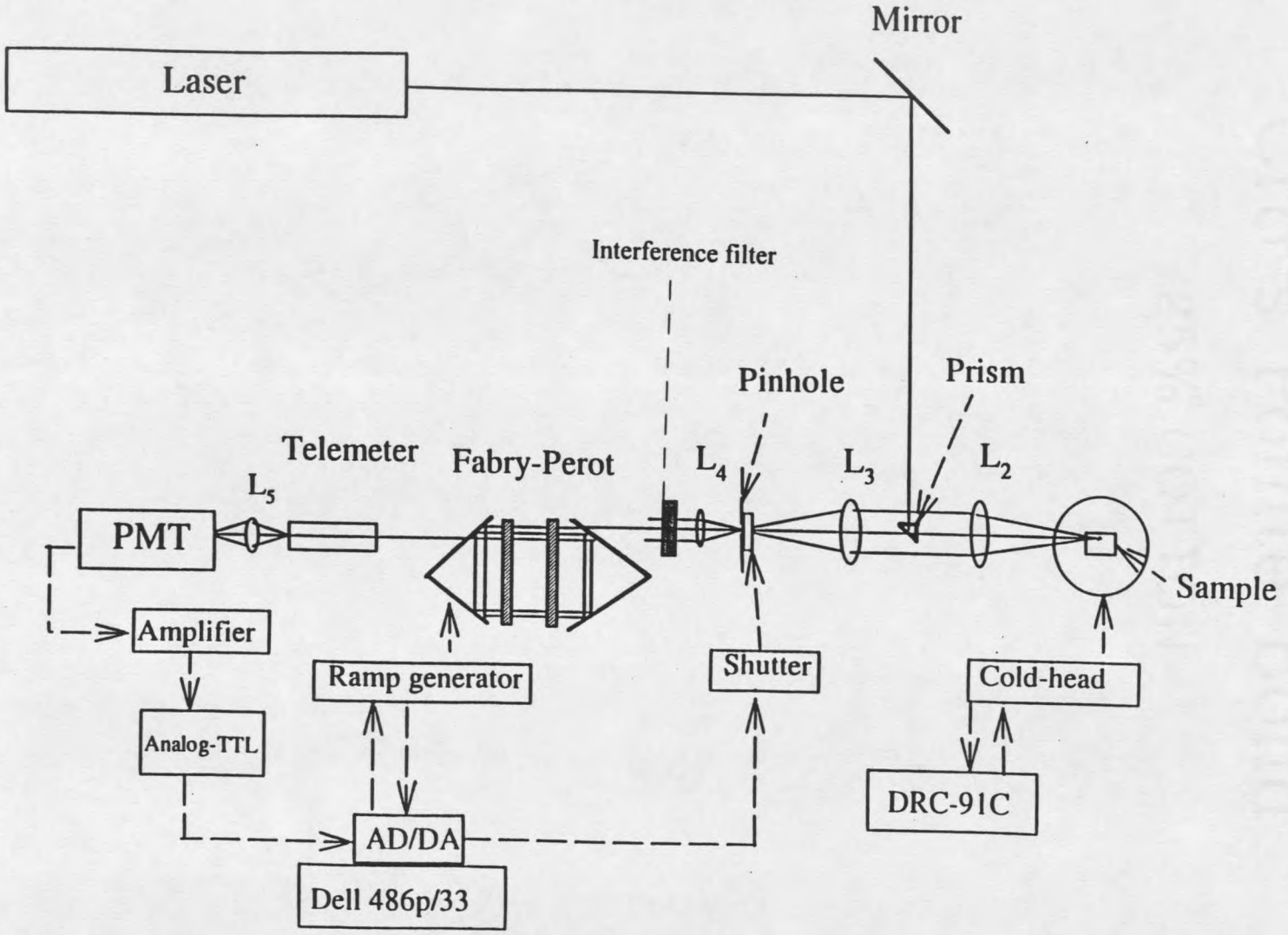

Figure 14 Brillouin scattering set-up for backscattering.

Fig. 14 is the experimental set-up for backscattering in which a 5×5 mm^2 prism was used to reflect the laser beam into L_3.

A LABTECH NOTEBOOK software was modified with an AD/DA converter to interface the shutter, TTL transformer and ramp function generator. A detailed connection scheme between converter and instruments is given in Fig. 15.

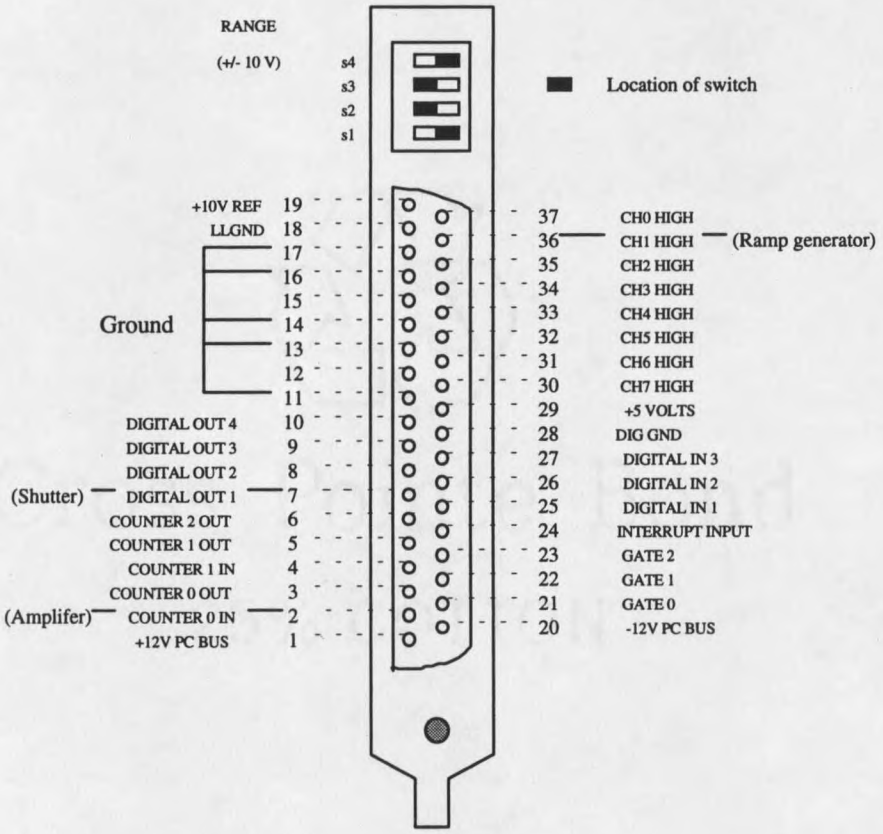

Figure 15. The actual experimental connection between AD/DA converter and instruments.

Before acquiring a Brillouin spectrum, an adjusting program whose operation was observed on the computer screen was used to optimize the spectrum by optimizing the intensity of the Rayleigh lines. Acquisition of spectra is accomplished under computer control. The frequency interval of each scan is about 1.2 free spectral range

(FSR), within which two elastic peaks (Rayleigh lines) were included. Usually, each scan took 100 or 200 s depending on the intensity of the signal. A typical Brillouin spectrum is given in Fig. 16. The two maxima on both sides are Rayleigh peaks and the two smaller peaks between them are the Brillouin components.

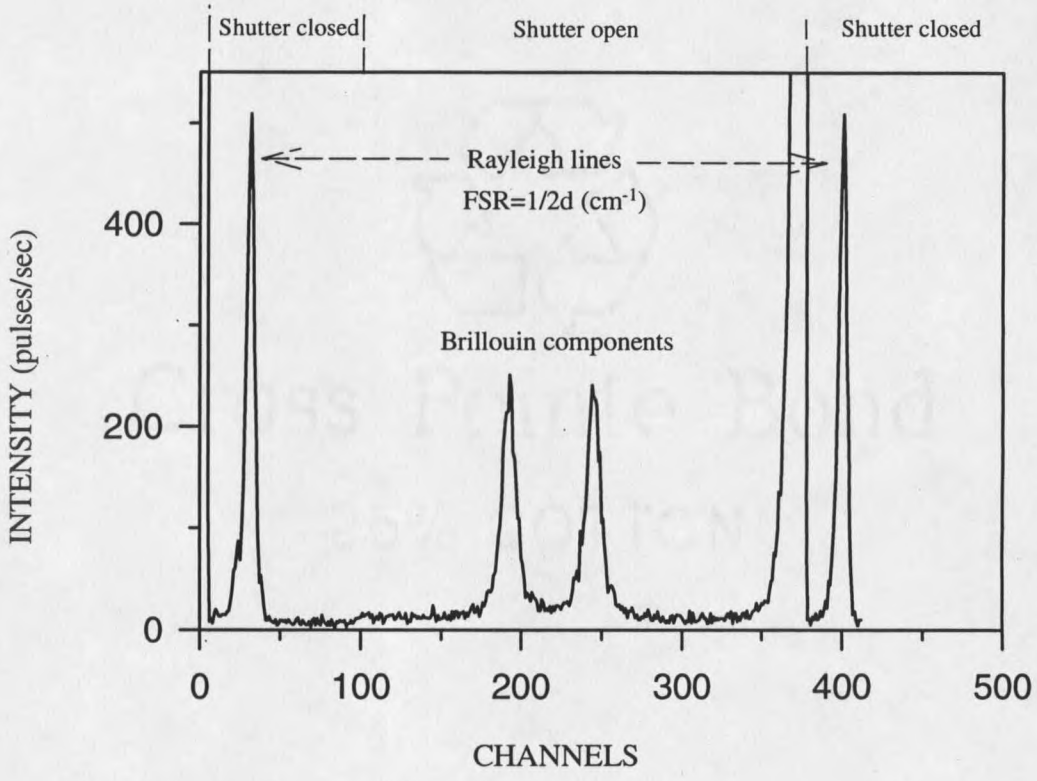

Figure 16. A typical Brillouin spectrum. d is the space between two mirrors of the Fabry-Perot interferometer. FSR means free spectral range.

A Leybold RGD-210 closed-cycle refrigerator which can operate from 10 to 475 K under vacuum ($<10^{-3}$ torr) was used for temperature control with a LakeShore DRC-91C temperature controller. Fig. 17 shows the relative positions of sample, sensor and light beam in the closed-cycle helium refrigerator.

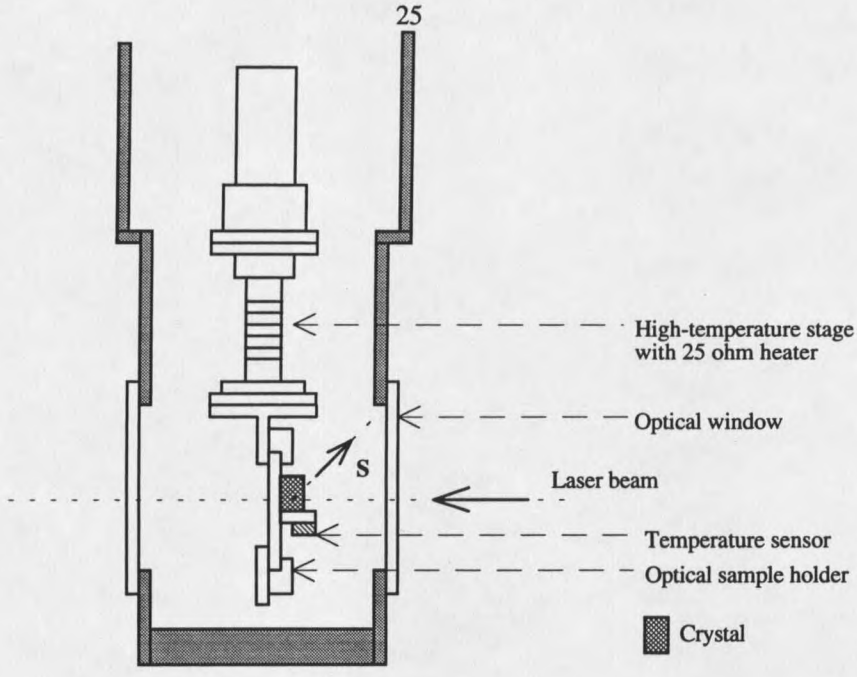

Figure 17. Actual positions of crystal, thermal sensor and laser beam in the closed-cycle helium refrigerator.

The temperature reading error was controlled to better than ±0.1 K and temperature was measured to ±0.01 K by using a calibrated silicon diode thermal sensor placed on the optical sample holder. For higher temperature (300-900 K), a closed oven with four windows was used with a calibrated LakeShore PT-103 platinum resistance thermometer and a manual controlled power supply. The temperature accuracy is about ±0.1 K.

Characteristics of the Fabry-Perot Interferometer[40]

The Fabry-Perot interferometer plays a key role in Brillouin light scattering. For better understanding of how the frequency shift and half-width were measured and determined, we briefly review its characteristics here.

The condition for constructive interference for a transmitted wave front is

$$2nd\cos\theta = m\lambda \qquad (3)$$

where n is the refractive index of the medium between the two reflecting mirror surfaces, d is the mirror spacing, and θ is the inclination of the normal of the mirror surface to the wave front direction. m is the order of interference and λ is the wavelength of the laser beam. In our case, the incident laser beam is perpendicular to the mirror surface (θ=0). Since the medium between the two mirrors is air, the refractive index is $n \cong 1$, Therefore, Eq. (3) becomes

$$d = \frac{m\lambda}{2} \tag{4}$$

If d decreases by $\lambda/2$, a wave with the same wavelength is still able to pass the interferometer but the order of the interference lowers by one. Also, there will be another wave with different wavelength that may pass but with the same m^{th} order interference. Hence we have

$$d = (m-1)\frac{\lambda_1}{2} = m\frac{\lambda_2}{2} \tag{5}$$

$$\delta\lambda = \lambda_1 - \lambda_2 \approx \frac{\lambda_1^2}{2d} \tag{6}$$

$\delta\lambda$ is called the free spectral range (FSR). In term of frequency ν,

$$2d = \frac{mc}{\nu_1} \tag{7}$$

$$2d = \frac{(m-1)c}{\nu_2} \tag{8}$$

where c is the speed of light. From Eqs. (7) and (8), one can obtain

$$\Delta\nu = \nu_1 - \nu_2 = \frac{c}{2d} \text{ (Hz)} \tag{9}$$

or

$$\Delta\nu = \frac{1}{2d} \text{ (cm}^{-1}\text{)} \qquad \text{(Note:1 cm}^{-1}\text{=30 GHz)} \tag{10}$$

Here $\Delta\nu$ is the frequency interval between two nearest bright interference fringes (or Rayleigh peaks) and also called the free spectral range (FSR).

Assume the optical length d changes by $\lambda_1/2\alpha$, where α is not an integer. The wave front of wavelength λ_3 is allowed to pass this interferometer if the following formula is satisfied:

$$2(d - \frac{\lambda_1}{2\alpha}) = (m - i)\lambda_3 \tag{11}$$

where m and i are integers. Then

$$\lambda_3 = \frac{2(d - \frac{\lambda_1}{2\alpha})}{\frac{2d}{\lambda_1} - i} \tag{12}$$

Here we have used the relation, $2d=m\lambda_1$. Then

$$\Delta\lambda = \lambda_3 - \lambda_1 = \frac{\lambda_1^2(i - \frac{1}{\alpha})}{2d(1 - \frac{i\lambda_1}{2d})} \tag{13}$$

Normally $m>>i$ and $2d>>i\lambda$ ($\lambda \sim 5\times10^{-5}$ cm), so

$$\Delta\lambda \approx \frac{\lambda_1^2(i-\frac{1}{\alpha})}{2d} = (i-\frac{1}{\alpha})\cdot FSR \tag{14}$$

or

$$\Delta\nu = (i-\frac{1}{\alpha})\cdot FSR \tag{15}$$

Here $\Delta\nu$ is the frequency shift from the original wave (Rayleigh line) and i is the shift order which is with respect to the Rayleigh line and is different from the order of interference. Experimental determination of shift order of Brillouin components will be discussed later in this chapter.

The Fabry-Perot interferometer which we used for experiments is a Burleigh Instr. Model RC-140. It uses matched sets of piezoelectric PZT transducers constructed from interferometrically matched PZT discs. This PZT material offers linearity and hysteresis characteristics better than 1% and 0.5%, respectively. The RC-42 Ramp Function Generator drives the FP interferometer. The ramp generator controls the PZT to provide two functions, i.e. scanning and alignment.

The finesse is the measurement of the interferometer's ability to resolve closely spaced lines (close frequencies). The finesse (F_1) for our system was about 40 (for single pass). For multi-pass system, the finesse is

$$F_p = \frac{F_1}{(2^p-1)^{\frac{1}{2}}} \tag{16}$$

where p is the number of passes. In our five-pass system, the finesse is about 104. The contrast of multi-pass system is also improved significantly.

Pre-Alignment of Fabry-Perot Interferometer

This is a rough parallel alignment procedure for Fabry-Perot mirrors and is critical for obtaining Brillouin spectrum. It should be completed before measurement. Before doing this pre-alignment, the ramp generator needs to be set at the following position: power "on", three biases "~one and half turn", ramp bias "~one quarter turn" and others "off". The cover of the Fabry-Perot interferometer must be removed and a piece of paper is placed in front of the front mirror as shown in Fig. 18a. A reflective mirror was used to reflect the interference pattern into the observer's eyes. How do you know that the two mirrors are on "rough" parallel position? The trick is to move the reflective mirror along the triangle indicated by dashed lines in Fig. 18b and adjust the two bigger knobs (labeled "L" and "R" in Fig. 18b) until the radius of the interference rings (shown in Fig. 19)[40] is almost constant everywhere.

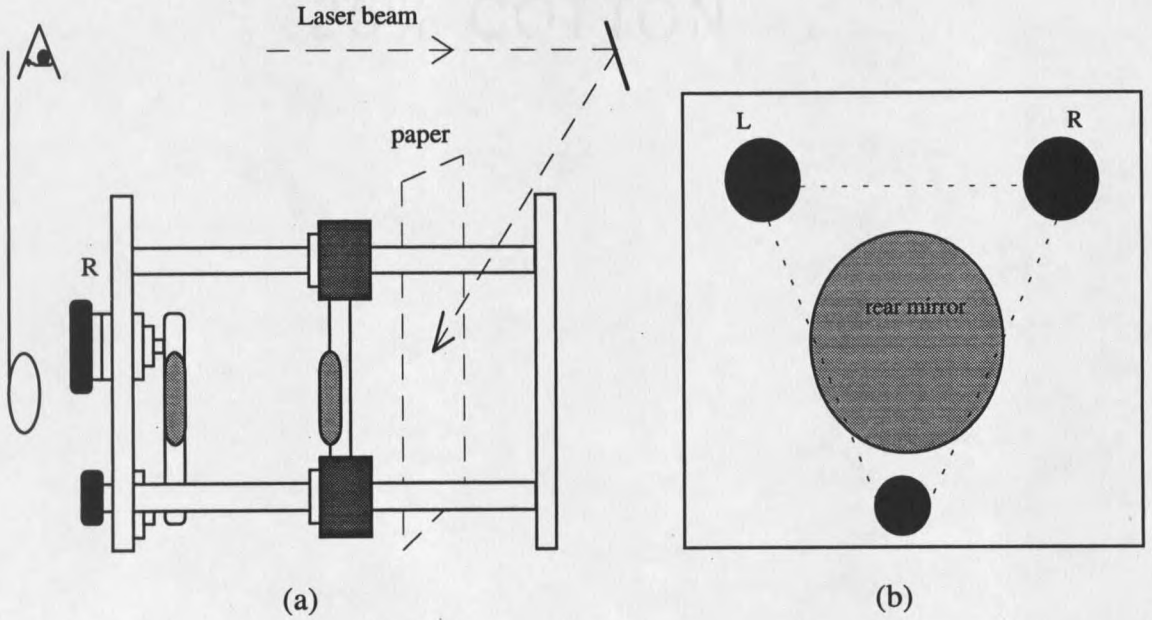

Figure 18. (a) A set-up for pre-alignment of the Fabry-Perot interferometer mirrors. (b) The dashed line indicates the path along which the reflective mirror is moved to check the radius of interference rings.

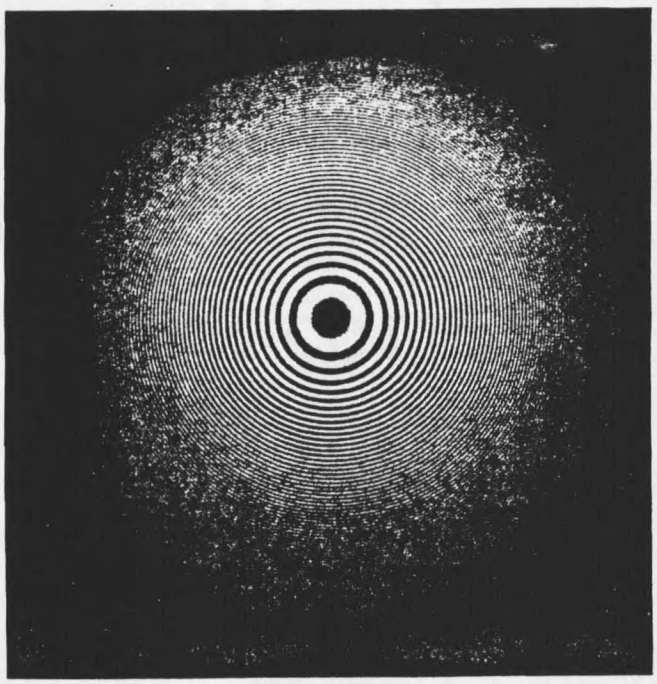

Figure 19. A typical transmitted interference pattern of a Fabry-Perot etalon.

Brillouin Spectrum Analysis

Typical traces of the Brillouin spectrum have been shown in Fig. 16. The determination of phonon frequency shift and half-width can be done by selecting a suitable FSR, i.e. suitable Fabry-Perot spacing d (FSR=1/2d cm^{-1}). One should avoid having the two Brillouin peaks close to each other so that they overlap, or separated too much so that they move into the "skirts" of the Rayleigh peaks. Since different materials have different values of frequency shift, a larger FSR (~$2cm^{-1}$=60 GHz) usually is chosen first in order to have the Brillouin peaks appearing in first order with respect to the Rayleigh peak (see Fig. 20a). With such a large FSR, one can easily determine the actual phonon frequency shift range. However, a large FSR will reduce the resolution of phonon half-width. Thus, a smaller FSR is preferred in actual measurement, so that the

Brillouin peaks appear in the higher (second or third) order with respect to the Rayleigh peak (see Fig. 20b).

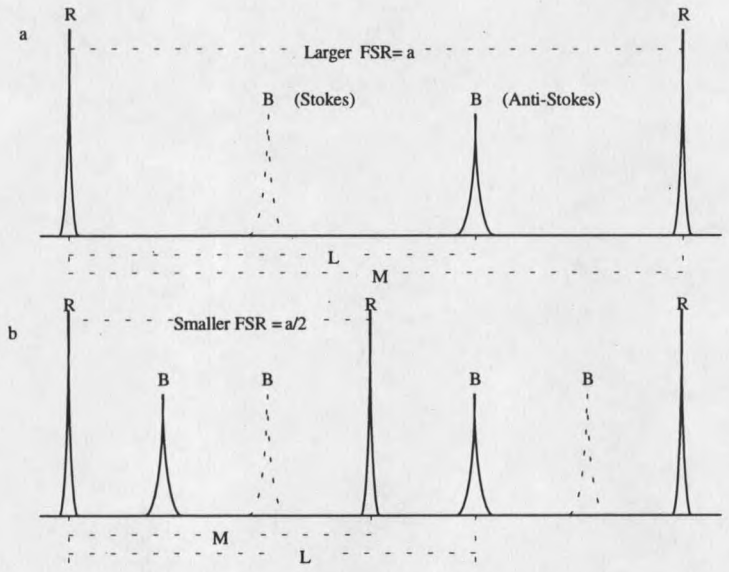

Figure 20. (a) An illustration of the Brillouin spectrum with larger FSR=α. R and B represent the Rayleigh and Brillouin components, respectively. (b) An illustration of the Brillouin spectrum with smaller FSR=$\alpha/2$.

The frequency shift can be determined by the following equation

$$\Delta\nu = \frac{L}{M}\mathrm{FSR} \tag{17}$$

where L is the total channel number between the Brillouin peak and Rayleigh line and M is the total channel number between the two nearest Rayleigh peaks. Here the Brillouin component has a half-width $\delta\nu$ (at half height) that arises from the finite lifetime of the phonons responsible for the scattering. A typical Lorentz profile equation which is a result of the assumption that phonons decay in time as $e^{-\delta\nu \cdot t}$, can be used to fit the spectrum, i.e.

$$I(x) = \frac{A}{B^2 + (x - C)^2} + D \tag{18}$$

where I(x) is the spectrum intensity and x is the channel number. D is the background intensity and A is an arbitrary number. From fitting, the frequency shift $\Delta\nu$ and observed half-width $\delta\nu_{obs}$ can be determined as

$$\Delta\nu = (N - 1 + \frac{C}{M}) \cdot FSR \tag{19}$$

$$\delta\nu_{obs} = \frac{2B}{M} \cdot FSR \tag{20}$$

where N is an integer (1, 2, 3 etc.). N=1 means that the Brillouin peak appears in first order with respect to the Rayleigh peak, and so on.

For determination of natural-phonon half-width $\delta\nu_{ph}$, the natural-phonon spectrum and the instrumental function were assumed to have a Lorentz distribution, and the broadening due to collection optics was assumed to have rectangular distribution. In this case, the natural-phonon half-width $\delta\nu_{ph}$ is given by[41]

$$\delta\nu_{ph} = \left(\delta\nu_{obs}^2 - \delta\nu_{ang}^2\right)^{\frac{1}{2}} - \delta\nu_{inst} \tag{21}$$

where $\delta\nu_{obs}$, $\delta\nu_{inst}$, and $\delta\nu_{ang}$ represent the observed, instrumental, and collection optical half-widths, respectively.

The Brillouin line broadening $\delta\nu_{ang}$ due to finite collection angle $\delta\theta_{ap}$ is described by a well-known formula which to second order in $\delta\theta$ is[42]

$$\frac{\delta\nu_{ang}}{\Delta\nu} = \frac{\cot(\frac{\theta}{2})\delta\theta_{ap}}{2} - \frac{(\delta\theta_{ap})^2}{8} \qquad (22)$$

where θ is the scattering angle and $\Delta\nu$ is the phonon frequency shift. In our case, $\delta\theta_{ap}$ is ~0.057 (radians) obtained from measurements of fused quartz. According to Eq. (22), the broadening problem is severe in near-forward scattering (or small scattering angles) for which $\cot(\theta/2)$ is large. The half-width of the Rayleigh line in fused quartz was taken as the instrumental broadening $\delta\nu_{ins}$.

CHAPTER 3

THEORY

Dielectric

The generally employed principle behind making measurements on a certain system is to subject it to a "force" and then examine how the system responds. In the dielectric case, the "force" is an electric field. In order to reflect the intrinsic properties of the system, the applied field should be "suitably small". In other words, the applied perturbation must not alter the nature of the system under study. This, in fact, is the essence of the linear response theory (LRT). Within this general framework two kinds of measurements may be performed: (i) response, in which the equilibrium value of some properties of the system under the influence of a time-independent field is measured, (ii) relaxation, in which a time-independent field that has been applied on the system for a long time is removed and the "free decay" of a system property such as polarization is investigated.

In dielectric materials, the intrinsic polarization is usually made up of three different components according to the nature of the charges displaced, i.e., electronic, ionic, and orientational (dipolar) polarizations. Only the dipolar contribution which comes from the reorientation of permanent dipoles, may lag the applied field and thus be responsible for dielectric dispersion at audio or radio frequencies. The other two

contributions (electronic and ionic) will become responsible for dispersion only if frequencies above 10^{12} Hz are applied.

Space charge (interfacial layers)[43] polarization is an extrinsic effect and usually arises from the presence of electrons or ions capable of migrating over distances of macroscopic magnitude. Some of these charge carriers tend to become trapped and accumulate at lattice defects, impurity centers, voids, or at electrode surfaces and so distort the field and produce an apparent increase in the dielectric permittivity.[43] Interfacial polarization is of particular importance in heterogeneous or multiphase (or multilayer) materials. Due to the differences in the electrical conductivity of the phases present, charges move through the more conducting phases and build up on the surfaces that separate these from the more resistive phases.

For large fields, nonlinear properties of polarization P against the electric field E are the characteristic of ferro- and antiferroelectrics, and other dielectrics to a smaller extent. At constant temperature, the electric field E can be expressed by the Taylor series expansion as[17]

$$\vec{E} = \frac{1}{\vec{\vec{\chi}}}\vec{P} + \varsigma\vec{P}^3 + \xi\vec{P}^5 \tag{23}$$

Here, $\vec{\vec{\chi}}$ is the static electric susceptibility. ς and ζ are coefficients of the dielectric nonlinearity. If the applied electric field is small enough, however, the higher order nonlinear terms will not be evident. This is the case that we will be dealing with here. So, we will limit ourselves to the treatment of linear dielectric media, i.e. $\vec{P} = \vec{\vec{\chi}}\vec{E}$.

The dielectric permittivity tensor ε_{ij} is defined from the relationship between electric field and electric displacement, i.e.

$$\vec{D}(t) = \varepsilon_o \vec{\vec{1}}\vec{E}(t) + \vec{P} = \varepsilon_o \vec{\vec{\varepsilon}}\vec{E}(t) \tag{24}$$

i.e.

$$D_i = \varepsilon_o \varepsilon_{ij} E_j \tag{25}$$

where ε_o is the MKS constant.

In the simplest case, i.e. a harmonic electric field $\vec{E} = \vec{E}_o e^{i\omega t}$ propagating in the material, the electric displacement can be given by

$$\vec{D}(\omega, T) = \vec{D}_o(T) e^{i(\omega t - \delta)} \tag{26}$$

i.e.

$$D_{oi}(T) e^{i\delta(\omega)} = \varepsilon_o \varepsilon_{ij}(\omega, T) E_{oj} \tag{27}$$

This expression allows us to define the complex dielectric permittivity as

$$\varepsilon^*_{ij}(\omega, T) = \varepsilon'_{ij}(\omega, T) - i\varepsilon''_{ij}(\omega, T) \tag{28}$$

i.e. $$\varepsilon'_{ij}(\omega, T) = \frac{D_{oi}(T)\cos\delta(\omega)}{\varepsilon_o E_{oj}}; \quad \varepsilon''_{ij}(\omega, T) = \frac{D_{oi}(T)\sin\delta(\omega)}{\varepsilon_o E_{oj}} \tag{29}$$

The quantity $\varepsilon''_{ij}(\omega)$ determines the component of D(t) with a phase difference of $\pi/2$ with respect to E(t) and can be easily shown to be proportional to the dissipated power density ($=\omega\varepsilon_o\varepsilon'' E_o^2/2$) in the dielectric. For this reason, $\varepsilon''(\omega)$ is also called the loss factor.

In the actual measurement, the capacitance C and conductance G were detected and then used in the following relationships to obtain complex dielectric permittivitty, i.e.

$$C^* = C - i\frac{G}{\omega} = \frac{\partial Q}{\partial V} = \frac{\partial(A\varepsilon_o\varepsilon^* E)}{\partial V} = \frac{\varepsilon_o A}{d}\varepsilon^* = C_o\varepsilon^*, \tag{30}$$

$$\varepsilon'_{ij}(\omega,T) = \frac{C_{ij}(\omega,T)}{C_o} \qquad \varepsilon''_{ij}(\omega) = \frac{G_{ij}(\omega,T)}{\omega C_o} \tag{31}$$

where $C_o = \varepsilon_o A / d$ is the geometrical capacitance, i.e., the capacitance that we would obtain from the parallel plate capacitor when the sample is removed. A is the sample area which is contacted with electrode and d is the sample thickness. $\omega = 2\pi f$ (Hz) is the angular frequency.

The elements of dielectric tensor ε^*_{ij} usually are anisotropic and depend on crystal symmetry. From thermodynamic arguments, we know that the dielectric permittivity tensor is symmetric, i.e. $\varepsilon^*_{ij} = \varepsilon^*_{ji}$. Following are different dielectric tensors which correspond to different crystal symmetries along some specific symmetry directions.[14]

Triclinic: $$\varepsilon^*_{ij} = \begin{bmatrix} \varepsilon^*_{11} & \varepsilon^*_{12} & \varepsilon^*_{13} \\ \varepsilon^*_{12} & \varepsilon^*_{22} & \varepsilon^*_{23} \\ \varepsilon^*_{13} & \varepsilon^*_{23} & \varepsilon^*_{33} \end{bmatrix}$$

Monoclinic: $$\varepsilon^*_{ij} = \begin{bmatrix} \varepsilon^*_{11} & \varepsilon^*_{12} & 0 \\ \varepsilon^*_{12} & \varepsilon^*_{22} & 0 \\ 0 & 0 & \varepsilon^*_{33} \end{bmatrix}$$ ($\hat{z}$ along the 2-fold axis)

Orthorhombic: $\varepsilon_{ij}^* = \begin{bmatrix} \varepsilon_{11}^* & 0 & 0 \\ 0 & \varepsilon_{22}^* & 0 \\ 0 & 0 & \varepsilon_{33}^* \end{bmatrix}$ (three 2-fold axes are axes)

Trigonal

and

Tetragonal: $\varepsilon_{ij}^* = \begin{bmatrix} \varepsilon_{11}^* & 0 & 0 \\ 0 & \varepsilon_{11}^* & 0 \\ 0 & 0 & \varepsilon_{33}^* \end{bmatrix}$ ($\hat{z}$ along the n-fold axis, n>2)

and

Hexagonal

Cubic: $\varepsilon_{ij}^* = \begin{bmatrix} \varepsilon_{11}^* & 0 & 0 \\ 0 & \varepsilon_{11}^* & 0 \\ 0 & 0 & \varepsilon_{11}^* \end{bmatrix}$

A cubic crystal is an isotropic dielectric medium, i.e. the elements of the dielectric tensor are diagonal and equal, and do not depend on any reference axis.[14]

Dipolar Relaxation Equations

For most practical cases, the dielectric relaxation behavior of reorienting dipoles can be described quantitatively by the following equation:

$$\varepsilon^*(\omega, T) = \varepsilon_\infty + \frac{\varepsilon_s - \varepsilon_\infty}{\left[1 + [i\omega\tau(T)]^{1-\alpha}\right]^\beta} \qquad (32)$$

The different values of parameters α and β are corresponding to different models. For practical purposes, three most useful empirical models are given below.

(1) Debye equation: $\alpha=0$, $\beta=1$[44]

In this equation, there is a single relaxation time τ. The real and imaginary parts of the dielectric permittivity can be separated as

$$\varepsilon'(\omega,T)=\varepsilon_\infty+\frac{\varepsilon_s-\varepsilon_\infty}{1+\omega^2\tau^2(T)},\quad \varepsilon''(\omega,T)=\frac{\omega\tau(T)(\varepsilon_s-\varepsilon_\infty)}{1+\omega^2\tau^2(T)} \tag{33}$$

The Cole-Cole plot of ε'' vs. ε' for various ω is a semicircle with its center at $(\varepsilon_\infty+\varepsilon_s)/2$ on the ε' axis.

(2) Cole-Cole equation: $0<\alpha<1$, $\beta=1$[44]

In this case, the inverse of the relaxation time τ has a frequency distribution. The real and imaginary parts of dielectric permittivity can be given by

$$\varepsilon'(\omega,T)=\varepsilon_\infty+\frac{1}{2}(\varepsilon_s-\varepsilon_\infty)\left[1+\frac{\sinh(1-\alpha)x}{\cosh(1-\alpha)x+\sin\frac{1}{2}\alpha\pi}\right] \tag{34}$$

$$\varepsilon''(\omega,T)=\frac{1}{2}(\varepsilon_s-\varepsilon_\infty)\left[\frac{\cos\frac{1}{2}\alpha\pi}{\cosh(1-\alpha)x+\sin\frac{1}{2}\alpha\pi}\right] \tag{35}$$

where $x=\ln(\omega_m/\omega)$. In these equations, $\omega_m\tau=1$ is the condition for the peak maximum in ε''. When plotting these equations in a Cole-Cole plot, we obtain a circular arc with its center lying below the real ε' axis and intersecting the ε' axis at angles of $\pi(1-\alpha)/2$ from a vertical line through the center.

(3) Cole-Davison equation: $\alpha=0$, $0<\beta<1$[44]

This description provides an asymmetric broadening (toward high frequencies) of a Debye peak by the introduction of the parameter β. In a Cole-Cole plot, this equation produces a right skewed arc.[5,44]

In term of frequency domain, these three different behaviors can be described as shown in Fig. 21.

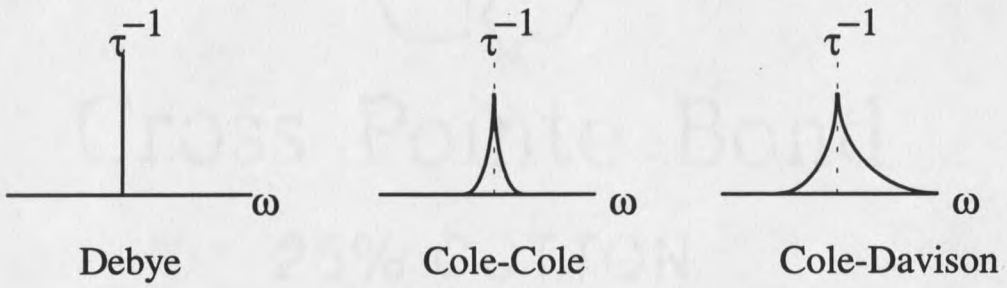

Figure 21. The Debye, Cole-Cole and Cole-Davison relaxation distribution functions.

Superparaelectric Model (nano-scale polar cluster)[16]

The behavior of dielectric permittivity in relaxor ferroelectrics usually is dependent on the size of polar cluster (or polar domain) which is induced by locally nonstoichiometric charged region. In the limit $N\rightarrow\infty$ (N is the number of dipole in a cluster), we would have a long-range-order ferroelectric phase transition which usually occurs at lower temperature. At high temperature, i.e. $N\rightarrow 1$, the real part of the dielectric permittivity ε' should obey the Curie law $\varepsilon'=1+p^2/(\varepsilon_o VkT)$. Here p is the dipole moment of a unit cubic cell, V is the cell volume, ε_o is the MKS constant, k is Boltzmann's constant and T is absolute temperature. At low temperature, if N remains finite (i.e. superparaelectric moment) instead of infinity, then the dc ε' should obey the N-dipole-cluster Curie law $\varepsilon'=Np^2/(\varepsilon_o VkT)$. In the following we will show a simple superparaelectric model in the DC limit.[16]

If we assume that each dipole interacts with the other dipoles in the same cluster, i.e. long-range interaction, then the Hamiltonian for one N-dipole cluster in an electric field E is

$$H = -\sum_{i=1}^{N}\left[pES_i + JS_i \sum_{j>i} S_j \right]$$

$$= -pE \sum_{i=1}^{N} S_i - \frac{J}{2}\left[\sum_{i=1}^{N} S_i \sum_{j=1}^{N} S_j - \sum_{k=1}^{N} S_k^2 \right]$$

$$= -pE \sum_{i=1}^{N} S_i - \frac{J}{2}\left(\sum_{i=1}^{N} S_i \right)^2 + \frac{NJ}{2} \qquad (36)$$

where J represents a positive (ferroelectric) interaction which for mathematical and computational simplicity is assumed to exist among all dipoles in the N-dipole cluster. p is the dipole moment of an unit cubic cell. We define n_+ as the number of dipole moment parallel to the field, i.e.

$$N = n_+ + n_-$$

$$\sum_{i=1}^{N} S_i = m = n_+ - n_- = 2n_+ - N \qquad (37)$$

Here we have assumed that each dipole has direction either along +z (↑) or -z (↓). "m" is the net dipole. Then, the partition function, Z, can be given by

$$Z = \sum_{n_+=0}^{N} \left(\frac{N}{n_+}\right) e^{\frac{pE}{kT}m + \frac{J}{2kT}(m^2 - N)} \qquad (38)$$

Usually, pE/kT is much smaller than 1, i.e.

$$e^{\frac{pE}{kT}m} \approx 1 + \frac{pE}{kT}m \qquad (39)$$

Therefore, the mean aligned dipole excess and dc dielectric permittivity are given by

$$\left\langle n_+ - n_- \right\rangle \equiv \langle m \rangle \approx 1 + \frac{\sum_{n_+=0}^{N} \frac{N!}{n_+!(N-n_+)!} \frac{pE}{kT} m^2 e^{\left(m^2-N\right)J/2kT}}{\sum_{n_+=0}^{N} \frac{N!}{n_+!(N-n_+)!} e^{\left(m^2-N\right)J/2kT}} \tag{40}$$

from Eq. (24), we have

$$\varepsilon'(f=0,T) = 1 + \frac{p<m>}{N\varepsilon_o EV} \tag{41}$$

where p<m>/NV is the cluster polarization. V is the unit cell volume ~$(4\text{Å})^3$.

If $(T-T_O)/T_O >> 2/N$, where $T_O \equiv NJ/k$, we can approximate the sum by an integral with limits extending to infinity, and replace the binomial coefficients by a gaussian, i.e.

$$\sum_{n_+=0}^{N} \frac{N!}{n_+!(N-n_+)!} \Rightarrow 2^N \sqrt{\frac{2}{N\pi}} \int_0^\infty e^{-\frac{(2n_+-N)^2}{2N}} dn_+ \qquad \left(dn_+ = \frac{1}{2} dm\right)$$

$$= 2^N \sqrt{\frac{2}{N\pi}} \int_0^\infty e^{-\frac{m^2}{2N}} dm \tag{42}$$

Here we use the relation

$$\left(\int_{-\infty}^{\infty} e^{-x^2} = 2 \int_0^\infty e^{-x^2} \right)$$

Therefore, Eq. (40) becomes

$$\langle m\rangle \approx \frac{\frac{pE}{kT}\int_0^\infty m^2 e^{\left(m^2-N\right)J/2kT-\frac{m^2}{2N}}\,dm}{\int_0^\infty e^{\left(m^2-N\right)J/2kT-\frac{m^2}{2N}}dm}$$

$$= \frac{\frac{pE}{kT}\int_0^\infty m^2 e^{-(\frac{1}{2N}-\frac{J}{2kT})m^2}\,dm}{\int_0^\infty e^{-(\frac{1}{2N}-\frac{J}{2kT})m^2}\,dm}$$

$$= \frac{pE}{2kT}(\frac{1}{2N}-\frac{J}{2kT})^{-1}$$

$$= \frac{pE}{4k}\cdot\frac{N}{T-T_o} \qquad (T_o \equiv NJ/k) \tag{43}$$

At higher temperature for which Eq. (43) is valid we obtain the Curie-Weiss law by substituting Eq. (43) into Eq. (41)

$$\varepsilon' \approx \frac{p^2}{4\varepsilon_o Vk(T-T_o)} \tag{44}$$

A dimensionless logarithmic derivative or "steepness parameter" S can be defined as

$$S \equiv \frac{T(\frac{d\varepsilon'}{dT})}{\varepsilon'} = \frac{d(\ln\varepsilon')}{d(\ln T)} \tag{45}$$

which is -1 in the Curie-law regions at very low and very high temperatures and which should have greatest magnitude near T_o.

Equivalent Circuits of Dielectric Function[43]

Strong dispersive dielectric behavior at low frequencies had been noted for a long time in many dielectric materials. As one knows, the interfacial effect also shows a strong dielectric frequency dispersion and could be reproduced by an equivalent circuit of capacitance in series with parallel G-C (see Fig. 22f).[43] This kind of inhomogeneous medium effect is already known under the general name of Maxwell-Wagner effect and it can be developed as a direct counterpart to the distributions of Debye-like relaxation behavior in a dipolar material. This model therefore, has all the superficial attraction, as well as all drawbacks of the distribution theories. Several equivalent circuits which represent several physical situations are given in Fig. 22. Following are some relations which might be helpful to understand Fig. 22.[43]

$$Z = Y^{-1} = R + \frac{-i}{\omega C} \quad \text{(for a series R-C circuit)}$$

$$Y = (\varepsilon'' + i\varepsilon')\omega\frac{\varepsilon_o A}{d} \quad \text{(for sample, A:area, d:thickness)}$$

$$C^* = C + i\frac{G}{\omega} \quad \text{and} \quad Y = G + i\omega C$$

Brillouin Light Scattering

Spectrum and Principle of Brillouin Scattering

In this section we will present a theory of Brillouin light scattering from the viewpoint of classical electromagnetism. For practical interest, we will be limited to the case of the radiation zone ($R \gg \lambda \gg r$), i.e., the wavelength of the emitted radiation λ (~ 5000 Å) is much greater than the dimension r (~1 Å) of the radiating source. R is the distance between observation point and origin. In this case, the vector potential $\vec{A}$ can be given by[45]

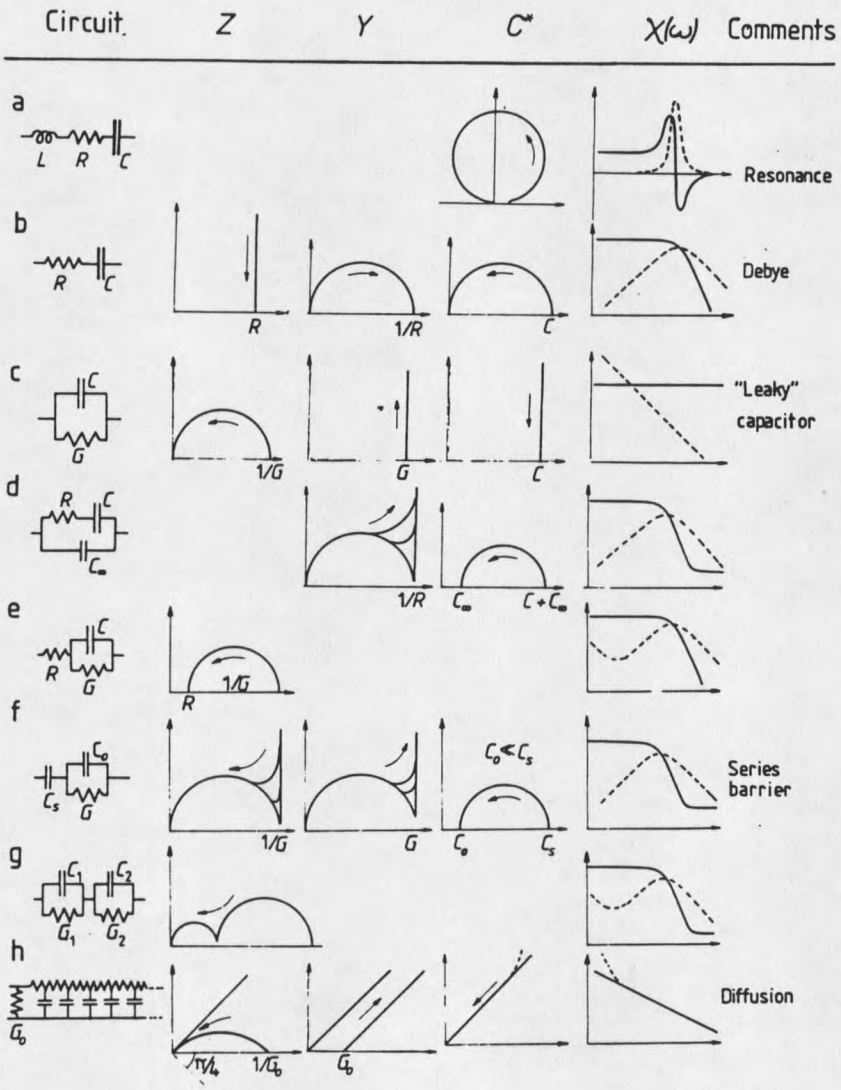

Figure 22. Schematic representations of the properties of simple circuit combinations of ideal, frequency-independent elements of capacitance C, conductance G or resistance R, and inductance L, as shown in first column. The second column gives the complex impedance plot Z, the third the complex admittance plot Y and the fourth the complex capacitance C*. The fifth column gives the corresponding plots of log C'(ω) (solid line) and log C"(ω) (dotted line), against log ω. Arrows indicate the sense of increasing frequency. Vertical and horizontal axes are imaginary and real parts, respectively.

$$\vec{A}(\vec{R},\omega)=\frac{e^{ikR}}{cR}\sum_{m=0}^{\infty}\frac{(-ik)^m}{m!}\int\vec{J}(\vec{r},\omega)(\hat{n}\cdot\vec{r})^m\,d^3r \qquad (46)$$

where $\hat{n}$ is the unit vector of $\vec{R}$. "r" is the position of the radiating source inside the medium. Since the terms of $k^m(\hat{n}\cdot\vec{r})^m$ go as $(d/\lambda)^m << 1$, the dominant term is for m=0 (dipole radiation). Then the vector potential becomes

$$\vec{A}(\vec{R},\omega)=\frac{e^{ikR}}{cR}\int\vec{J}(\vec{r},\omega)d^3r$$

$$=-ik\frac{e^{ikR}}{cR}\vec{P}(r,\omega);\qquad [\int\vec{J}(\vec{r},\omega)d^3r=-i\omega\int\vec{r}\rho(\vec{r},\omega)d^3r] \qquad (47)$$

with

$$\vec{P}=\int\vec{r}\rho(\vec{r},\omega)d^3r \qquad (48)$$

$\vec{P}$ is the electric dipole moment. In the radiation zone, the fields are $\vec{B}=\nabla\times\vec{A}$ and $\vec{E}=\vec{B}\times\hat{n}$, i.e.

$$\vec{E}(\vec{R},t)=\frac{1}{R}\hat{n}\times\left[\frac{\omega^2}{c^2}\int\vec{r}\rho(\vec{r},\omega)e^{-i\omega(t-\frac{R}{c})}d^3r\right]\times\hat{n}$$

$$=\frac{1}{c^2R}\hat{n}\times[\hat{n}\times\frac{\partial^2\vec{P}(t')}{\partial t'^2}] \qquad (49)$$

Here we use the relation $\vec{E}(\vec{R},t)=\vec{E}(\vec{R},\omega)e^{-i\omega t}$. $t'=t-\frac{n|\vec{R}-\vec{r}|}{c}\approx t-\frac{nR}{c}$ is the retarded time inside the medium. If the incident light intensity is weak, then the local polarization would be written approximately by

$$\vec{P} = \ddot{\alpha} \cdot \vec{E}_{in} \tag{50}$$

where $\ddot{\alpha}$ is the tensor of polarizability. $\vec{E}_{in}$ is the electric field of the incident wave within the medium. If it is a plane-wave field, then

$$\vec{E}_{in}(\vec{r},t) = \vec{E}_o e^{i(\vec{k}_o \cdot \vec{r} - \omega_o t)} \tag{51}$$

where $k_o = n\omega_o / c$ is the wave vector of the light wave and n is the refractive index of the medium. A light scattering diagram is shown in Fig. 23.

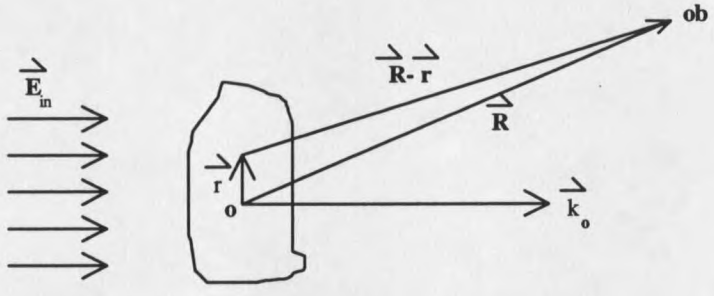

Figure 23. Light scattering diagram.

To analyze the origin of the scattering, it is convenient to decompose α into its time average part $<\alpha>$ and the time-space fluctuations $\delta\alpha(\vec{r},t)$ produced by the thermal fluctuations in the medium. The thermal fluctuations cause off-diagonal components to appear in the polarizability tensor, so we have

$$\vec{p}(\vec{r},t') = \left[< \ddot{\alpha} > + \delta\ddot{\alpha}(\vec{r},t') \right] \cdot \vec{E}_o e^{i(\vec{k}_o \cdot \vec{r} - \omega_o t')} \tag{52}$$

$$\frac{d\vec{P}}{dt'} = \left[-i\omega_o < \ddot{\alpha} > -i\omega_o \delta\ddot{\alpha} + \frac{d(\delta\ddot{\alpha})}{dt'} \right] \cdot \vec{E}_o e^{i(\vec{k}_o \cdot \vec{r} - \omega_o t')} \tag{53}$$

$$\frac{d^2\vec{P}}{dt'^2}=\left[-\omega_o{}^2<\vec{\alpha}>-\omega_o{}^2\delta\vec{\alpha}-2i\omega_o\frac{d(\delta\vec{\alpha})}{dt'}+\frac{d^2(\delta\vec{\alpha})}{dt'^2}\right]\cdot\vec{E}_o e^{i(\vec{k}_o\cdot\vec{r}-\omega_o t')} \qquad (54)$$

Since the characteristic frequencies of thermal fluctuations are small ($\leq 10^{13}$ Hz) compared to the light frequency in the optical region (~10^{15} Hz), we can regard $\delta\alpha$ as a very weak function of time, i.e.

$$\frac{d^2\vec{P}}{dt'^2}\approx\left[-\omega_o{}^2<\vec{\alpha}>-\omega_o{}^2\delta\vec{\alpha}\right]\cdot\vec{E}_o e^{i(\vec{k}_o\cdot\vec{r}-\omega_o t')}=-\omega_o{}^2\vec{P}(\vec{r},t') \qquad (55)$$

Substituting Eqs. (54) and (55) into Eq. (49) and carrying out the integration over the illuminated volume V at the retarded time t', we obtain

$$\vec{E}^{\text{Total}}=\int_v\vec{E}(\vec{R},t)d^3r=-\left(\frac{\omega_o}{c}\right)^2\frac{1}{R}\hat{n}\times\left[\hat{n}\times\int_V[<\vec{\alpha}>+\delta\vec{\alpha}]\cdot\vec{E}_o e^{i[\vec{k}_o\cdot\vec{r}-\omega_o(t-\frac{n|\vec{R}-\vec{r}|}{c})]}d^3r\right]$$

$$=-\left(\frac{\omega_o}{c}\right)^2\frac{1}{R}\hat{n}\times\left[\hat{n}\times\int_V[<\vec{\alpha}>+\delta\vec{\alpha}]\cdot\vec{E}_o e^{i(\vec{k}_o\cdot\vec{r}-\omega_o t)+i\vec{K}'\cdot(\vec{R}-\vec{r})}d^3r\right] \qquad (56)$$

Here we have used the relations

$$\vec{K}'=\frac{n\omega_o}{c}\hat{n};\qquad \hat{n}\approx\frac{\vec{R}-\vec{r}}{|\vec{R}-\vec{r}|} \qquad (57)$$

The integral in Eq. (56) gives the superposition of phases of waves scattered from each illuminated point in the crystal. The contribution to the integral from the $<\vec{\alpha}>$ term is zero except in the forward direction. This light oscillates at the same frequency as the

incident field and results only in elastic scattering. Scattering out of the incident direction results entirely from fluctuations $\delta\vec{\alpha}$ in the polarizability.

We can decompose the fluctuations into their spatial Fourier components

$$\delta\vec{\alpha}(\vec{r},t') = \left(\frac{1}{2\pi}\right)^{\frac{3}{2}} \sum_{\mu} \int \delta\vec{\alpha}(\vec{q}) e^{i\left[\vec{q}\cdot\vec{r} \pm \omega_{\mu}(\vec{q})(t - \frac{n|\vec{R}-\vec{r}|}{c})\right]} d^3q \qquad (58)$$

where $\vec{q}$ is the wave-vector of the fluctuation and $\omega_{\mu}(\vec{q})$ is the frequency of the fluctuation corresponding to this wave vector, i.e. $\omega_{\mu}(\vec{q}) = c|\vec{q}|$. The index μ denotes the possibility of a number of branches in the dispersion. In general, $\omega_{\mu}(\vec{q})$ can be complex to include a description of the damping of the fluctuation. $\omega_{\mu}(\vec{q})$ is double-valued with $\pm$ for the degeneracy in the dispersion for positive and negative running waves.

$$\vec{E}_{\text{scatt.}}^{\text{Total}} = -\left(\frac{1}{2\pi}\right)^{\frac{3}{2}} \left(\frac{\omega_o}{c}\right)^2 \frac{1}{R} \sum_{\mu} \hat{n} \times \left[\hat{n} \times \int_V \int_{\vec{q}} \delta\vec{\alpha}(\vec{q}) \cdot \vec{E}_o e^{i(\vec{k}_o\cdot\vec{r} - \omega_o t) + i\vec{K}'\cdot(\vec{R}-\vec{r})} e^{i[\vec{q}\cdot\vec{r} \pm \omega_{\mu}(\vec{q})t \mp \frac{n\omega_{\mu}(\vec{q})|\vec{R}-\vec{r}|}{c}]} d^3r d^3q \right] \qquad (59)$$

The exponential part of Eq. (59) can be rearranged as

$$e^{i(\vec{k}_o\cdot\vec{r} - \omega_o t) + i\vec{K}'\cdot(\vec{R}-\vec{r})} e^{i[\vec{q}\cdot\vec{r} \pm \omega_{\mu}(\vec{q})t \mp \frac{n\omega_{\mu}(\vec{q})|\vec{R}-\vec{r}|}{c}]}$$

$$= e^{i(\vec{k}_o\cdot\vec{r} - \omega_o t) + i\vec{K}'\cdot(\vec{R}-\vec{r})} e^{i[\vec{q}\cdot\vec{r} \pm \omega_{\mu}(\vec{q})t \mp \vec{k}_{\mu}\cdot(\vec{R}-\vec{r})]}$$

$$= e^{i[\vec{k}_o\cdot\vec{r} - \omega_o t]} e^{i[\vec{q}\cdot\vec{r} \pm \omega_{\mu}(\vec{q})t]} e^{i[(\vec{K}' \mp \vec{k}_{\mu})\cdot(\vec{R}-\vec{r})]}$$

$$= e^{i[\vec{k}_o \cdot \vec{r} - \omega_o t]} e^{i[\vec{q} \cdot \vec{r} \pm \omega_\mu(\vec{q})t]} e^{i[\vec{K} \cdot (\vec{R} - \vec{r})]}$$

$$= e^{i[\vec{K} \cdot \vec{R} - (\omega_o \mp \omega_\mu(\vec{q}))t]} e^{i[\vec{k}_o + \vec{q} - \vec{K}] \cdot \vec{r}} \tag{60}$$

Here we have used $\vec{k}_\mu = \frac{n\omega_\mu}{c}\hat{n}$ and $\vec{K} = \vec{K}' \pm \vec{k}_\mu$. Thus

$$\vec{E}_{scatt}^{Total} = -\left(\frac{1}{2\pi}\right)^{\frac{3}{2}}\left(\frac{\omega_o}{c}\right)^2 \frac{1}{R}\sum_\mu \hat{n} \times \left[\hat{n} \times \int_V \int_{\vec{q}} \delta\vec{\alpha}(\vec{q}) \cdot \vec{E}_o e^{i[\vec{K} \cdot \vec{R} - (\omega_o \mp \omega_\mu(\vec{q}))t]} e^{i[\vec{k}_o + \vec{q} - \vec{K}] \cdot \vec{r}} d^3r d^3q \right]$$

$$= -\left(\frac{\omega_o}{c}\right)^2 \frac{1}{R}\sum_\mu \hat{n} \times \left[\hat{n} \times \int_{\vec{q}} \delta\vec{\alpha}(\vec{q}) \cdot \vec{E}_o e^{i[\vec{K} \cdot \vec{R} - (\omega_o \mp \omega_\mu(\vec{q}))t]} d^3q \cdot \left(\frac{1}{2\pi}\right)^{\frac{3}{2}} \int_V e^{i[\vec{k}_o + \vec{q} - \vec{K}] \cdot \vec{r}} d^3r \right]$$

$$= -\left(\frac{\omega_o}{c}\right)^2 \frac{1}{R}\sum_\mu \hat{n} \times \left[\hat{n} \times \int_{\vec{q}} \delta\vec{\alpha}(\vec{q}) \cdot \vec{E}_o e^{i[\vec{K} \cdot \vec{R} - (\omega_o \mp \omega_\mu(\vec{q}))t]} d^3q \cdot (2\pi)^{\frac{3}{2}} \delta(\vec{k}_o + \vec{q} - \vec{K}) \right]$$

$$= -(2\pi)^{\frac{3}{2}}\left(\frac{\omega_o}{c}\right)^2 \frac{1}{R}\sum_\mu \hat{n} \times \left[\hat{n} \times \delta\vec{\alpha}(\vec{q}) \vec{E}_o e^{i[\vec{K} \cdot \vec{R} - (\omega_o \mp \omega_\mu(\vec{q}))t]} \right]_{\vec{q} = \vec{K} - \vec{k}_o} \tag{61}$$

We have used the delta function relation, i.e.

$$\int_V e^{i[\vec{k}_o + \vec{q} - \vec{K}] \cdot \vec{r}} d^3r = (2\pi)^3 \delta(\vec{k}_o + \vec{q} - \vec{K}) \tag{62}$$

Thus the wave vector which produces the scattering in the direction $\hat{n}$ is that which satisfies the implicit equation

$$\vec{q} = \vec{K} - \vec{k}_o \tag{63}$$

$$\left|\vec{K}\right| = K = \frac{n}{c}(\omega_o \pm \omega_\mu) = \frac{n\omega_s}{c} \tag{64}$$

where $\vec{K}$ is the wave vector of the scattered photon and $\vec{k}_o$ is the wave vector of the incident photon. $\vec{q}$ is the wave vector of the lattice fluctuation. Eqs. (63) and (64) represent the conservation of momentum among these three wave vectors, and conservation of energy, respectively. The plus and minus signs correspond to the so called anti-Stokes and Stokes lines in the spectrum, respectively. Momentum conservation among photons and phonon is illustrated in Fig. 24.

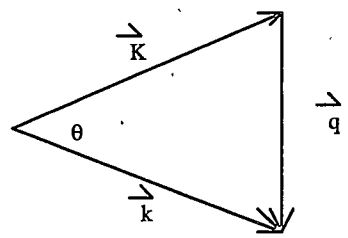

Figure 24. Momentum conservation of photons and phonon.

In Eq. (64), there are three $\omega_\mu(\vec{q})$ for the same wave vector $\vec{q}$, i.e. one longitudinal and two transverse modes. The $\hat{n}\times\hat{n}\times\delta\ddot{\alpha}(\vec{q})$ term gives the polarization of the scattered radiation. The same constraints can be derived by viewing the phonons as moving diffraction gratings (due to density fluctuation) with a velocity $V=\omega/q$, and the incident photons undergo Bragg reflection and Doppler shift.[36]

From Eq. (63), we can calculate the magnitude of the wave vector $\vec{q}$, i.e.

$$q^2 = K^2 + k_o^2 - 2Kk_0\cos\theta$$

$$= \left(\frac{n_s\omega_s}{c}\right)^2 + \left(\frac{n_i\omega_o}{c}\right)^2 - \frac{2n_in_s\omega_s\omega_o}{c^2}\cos\theta, \qquad (65)$$

where n_i and n_s are refractive indices for incident and scattered light respectively.

Because of $\omega_\mu << \omega_o$ ($\omega_\mu/\omega_o \sim 10^{-5}$), so we have $\omega_s \sim \omega_o$, i.e.

$$q = \frac{\omega_o}{c}(n_i^2 + n_s^2 - 2n_i n_s \cos\theta)^{\frac{1}{2}}. \tag{66}$$

In an optically isotropic medium such as a cubic system, the index ellipsoid is a sphere $[(x_1^2 + x_2^2 + x_3^2)/\varepsilon = 1]$ and $n_i = n_s = n$.[14] Then Eq. (66) becomes

$$q = \frac{2n\omega_o}{c}(\frac{1}{2} - \frac{1}{2}\cos\theta)^{\frac{1}{2}} = \frac{2n\omega_o}{c}\sin\frac{\theta}{2}, \tag{67}$$

$$q \equiv \frac{2\pi\Delta\nu}{V}, \qquad (\omega_o \equiv 2\pi\nu_o) \tag{68}$$

where V is the phonon velocity (sound velocity) and $\Delta\nu$ is the phonon frequency (or Brillouin frequency shift). From Eqs. (67) and (68), we have

$$\frac{\Delta\nu}{\nu} = \frac{V}{c}2n\sin\frac{\theta}{2}. \tag{69}$$

In an anisotropic medium, the index ellipsoid shown in Fig. 25 has important properties. The directions (polarizations) of the electric displacement vectors $\vec{D}_1$ and $\vec{D}_2$ of two waves are along the semi-axes of the ellipse obtained from the cross section of the index ellipsoid inside the crystal with the equatorial plane which is perpendicular to the wave vector. The indices are equal to the lengths of the semi-axes of the ellipse.[14]

For optically biaxial crystals (triclinic, monoclinic and orthorhombic systems), the three principal axes of an ordinary ellipsoid are 2-fold rotation axes. An ordinary ellipsoid $[x_1^2/n_1^2 + x_2^2/n_2^2 + x_3^2/n_3^2 = 1,\ n_1 \neq n_2 \neq n_3]$ has two circular equatorial cross sections which are symmetric with respect to two of the principal axes and which contain

the third axis. The directions orthogonal to these particular cross sections are the optical axes, i.e. only one index remains (the radius of the circle), waves with all polarization directions have the same velocity and there is no double refraction.

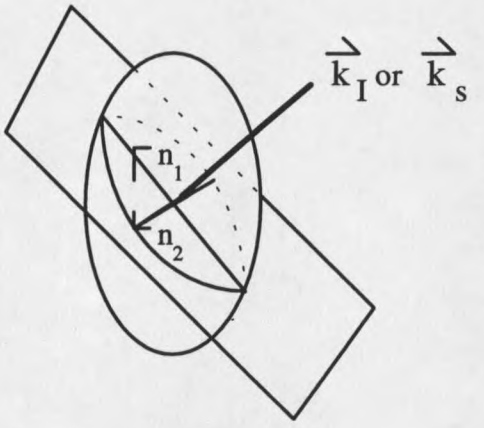

Figure 25. Index ellipsoid. Two waves, polarized along $\bar{D}_1$ and $\bar{D}_2$ (mutually orthogonal), can propagate in the $\bar{k}$ direction (applicable to both incident and scattered beams), with different velocities.

For optically uniaxial crystals (trigonal, tetragonal and hexagonal systems), one of the principal axes is a n-fold rotation axis A_n (n>2) and is the axis of revolution of the index ellipsoid. If the propagation direction is along A_n, the cross section of the index ellipsoid is a circular section, so the index is the same for any polarization direction. Thus the crystal will behave as an isotropic material for a wave propagating along A_n which is the optical axis. In this case, the equation for the index ellipsoid is $[(x_1^2 + x_2^2)/n_o^2 + x_3^2/n_e^2 = 1]$.[14]

In Brillouin scattering, one might worry about the problem of different indices and velocities inside the crystal caused by optical anisotropy. However, the difference between the principal indices is always small. The index ellipsoid is very close to a sphere. For instance, the indices of quartz are n_o=1.5442 and n_e=1.5533.[14]

The Relation Between Sound Velocity and Elastic Stiffness[14]

Brillouin scattering is a tool for measurement of elastic constants (stiffness) and piezoelectric stress constants. The calculation presented here is a basic theory for a non-piezoelectric material. The dynamic equation of lattice motion for a phonon can be written as[14]

$$\rho \frac{d^2 u_i}{dt^2} = \frac{dT_{ij}}{dx_j} \tag{70}$$

where u_i is the displacement in the i^{th} direction, ρ is the crystal density and T_{ij} are elements of the stress tensor. One can use the generalized Hooke's law to form the relation between the stresses and the strains, i.e.[14]

$$T_{ij} = C^E_{ijkl} S_{kl} \qquad (i,j,k,l=1,2,3 \text{ or } x,y,z) \tag{71}$$

and

$$S_{kl} = \frac{1}{2}\left(\frac{du_k}{dx_l} + \frac{du_l}{dx_k}\right) \tag{72}$$

where the C^E_{ijkl} are the elastic stiffness constants (Young's Modulus) at constant electric field and S_{kl} are the strain components. Substituting Eqs. (71) and (72) into Eq. (70) yields the phonon wave equations

$$\rho \frac{d^2 u_i}{dt^2} = C_{ijkl} \frac{1}{2} \frac{d}{dx_j}\left(\frac{du_k}{dx_l} + \frac{du_l}{dx_k}\right) \tag{73}$$

One can exchange "k" and "l" symbols, i.e.

$$C^{E}_{ijkl}\frac{d}{dx_j}\frac{du_l}{dx_k} \Rightarrow C^{E}_{ijlk}\frac{d}{dx_j}\frac{du_k}{dx_l}$$

Since elastic stiffness constants is a symmetry tensor,

$$C^{E}_{ijkl} = C^{E}_{ijlk},$$

and Eq. (73) becomes

$$\rho\frac{d^2u_i}{dt^2} = C^{E}_{ijkl}\frac{d^2u_k}{dx_j dx_l}. \tag{74}$$

We seek plane-wave solutions of the phonon equation of motion in which the displacement vector can be written as

$$u_i = u_{io}e^{i(\vec{q}.\vec{r}-\omega t)}, \qquad \omega\equiv 2\pi\Delta\nu \text{ (Brillouin shift)} \tag{75}$$

where u_{io} is the displacement and i is the polarization index of the phonon. From Eqs. (68) and (74), we have

$$\rho V^2 u_i = C^{E}_{ijkl} I_j I_l u_k \tag{76}$$

where V is the sound velocity. I_j and I_l are the components (projections) of the unit phonon wave vector $\hat{q}=\vec{q}/|q|$ along the j- and l-axes. From now on, we will omit the superscript "E" for elastic stiffness constants, i.e. $C_{ijkl} \equiv C^{E}_{ijkl}$.

For i=1, from Eq. (76) one has

$$\begin{aligned}\rho V^2 u_1 = {} & C_{1111}I_1I_1u_1 + C_{1112}I_1I_2u_1 + C_{1113}I_1I_3u_1 \\ & + C_{1121}I_1I_1u_2 + C_{1122}I_1I_2u_2 + C_{1123}I_1I_3u_2 \\ & + C_{1131}I_1I_1u_3 + C_{1132}I_1I_2u_3 + C_{1133}I_1I_3u_3 \\ & + C_{1211}I_2I_1u_1 + C_{1212}I_2I_2u_1 + C_{1213}I_2I_3u_1 \\ & + C_{1221}I_2I_1u_2 + C_{1222}I_2I_2u_2 + C_{1223}I_2I_3u_2 \\ & + C_{1231}I_2I_1u_3 + C_{1232}I_2I_2u_3 + C_{1233}I_2I_3u_3 \\ & + C_{1311}I_3I_1u_1 + C_{1312}I_3I_2u_1 + C_{1313}I_3I_3u_1 \\ & + C_{1321}I_3I_1u_2 + C_{1322}I_3I_2u_2 + C_{1323}I_3I_3u_2 \\ & + C_{1331}I_3I_1u_3 + C_{1332}I_3I_2u_3 + C_{1333}I_3I_3u_3 \end{aligned} \tag{77}$$

It is more convenient to use matrix notation than tensor notation, i.e.

Tensor notation:	11	22	33	23,32	13,31	12,21
Matrix notation:	1	2	3	4	5	6

After changing tensor to matrix notation, Eq. (77) becomes

$$\begin{aligned}\rho V^2 u_1 = {} & C_{11}I_1I_1u_1 + C_{16}I_1I_2u_1 + C_{15}I_1I_3u_1 \\ & + C_{16}I_1I_1u_2 + C_{12}I_1I_2u_2 + C_{14}I_1I_3u_2 \\ & + C_{15}I_1I_1u_3 + C_{14}I_1I_2u_3 + C_{13}I_1I_3u_3 \\ & + C_{61}I_2I_1u_1 + C_{66}I_2I_2u_1 + C_{65}I_2I_3u_1 \\ & + C_{66}I_2I_1u_2 + C_{62}I_2I_2u_2 + C_{64}I_2I_3u_2 \\ & + C_{65}I_2I_1u_3 + C_{64}I_2I_2u_3 + C_{63}I_2I_3u_3 \\ & + C_{51}I_3I_1u_1 + C_{56}I_3I_2u_1 + C_{55}I_3I_3u_1 \\ & + C_{56}I_3I_1u_2 + C_{52}I_3I_2u_2 + C_{54}I_3I_3u_2 \\ & + C_{55}I_3I_1u_3 + C_{54}I_3I_2u_3 + C_{53}I_3I_3u_3 \end{aligned} \tag{78}$$

The elastic stiffness constant tensor depends on the crystal symmetry and the reference frames. For orthorhombic (for all classes if three orthogonal diad axes are chosen as the reference frame), cubic (for all classes) and tetragonal (for classes 4mm,

$\bar{4}2m$, 422 and 4/mmm if the 4-fold rotation axis and two orthogonal diad axes are chosen as the reference frame), the elastic stiffness constant matrix can be expressed as[14]

$$C_{ij}=\begin{bmatrix} C_{11} & C_{12} & C_{13} & 0 & 0 & 0 \\ C_{12} & C_{22} & C_{23} & 0 & 0 & 0 \\ C_{13} & C_{23} & C_{33} & 0 & 0 & 0 \\ 0 & 0 & 0 & C_{44} & 0 & 0 \\ 0 & 0 & 0 & 0 & C_{55} & 0 \\ 0 & 0 & 0 & 0 & 0 & C_{66} \end{bmatrix}$$

The 6×6 coefficients C_{ij} are symmetric with respect to the main diagonal. Thus, Eq. (78) becomes

$$\begin{aligned} \rho V^2 u_1 = & (C_{11}I_1I_1 + C_{55}I_3I_3 + C_{66}I_2I_2)u_1 \\ & +(C_{12}I_1I_2 + C_{66}I_2I_1)u_2 \\ & +(C_{13}I_1I_3 + C_{55}I_3I_1)u_3 \end{aligned} \tag{79}$$

Similarly, for i=2 and 3, we have

$$\begin{aligned} \rho V^2 u_2 = & (C_{66}I_1I_2 + C_{12}I_2I_1)u_1 \\ & +(C_{66}I_1I_1 + C_{22}I_2I_2 + C_{44}I_3I_3)u_2 \\ & +(C_{23}I_2I_3 + C_{44}I_3I_2)u_3 \end{aligned} \tag{80}$$

$$\begin{aligned} \rho V^2 u_3 = & (C_{55}I_1I_3 + C_{13}I_3I_1)u_1 \\ & +(C_{44}I_2I_3 + C_{23}I_3I_2)u_2 \\ & +(C_{44}I_2I_2 + C_{33}I_3I_3 + C_{55}I_1I_1)u_3 \end{aligned} \tag{81}$$

For non-trivial solutions of this set of Eqs. (79), (80) and (81), the following determinant of the coefficient matrix must vanish for an arbitrary phonon wave direction $\vec{q}$ in the

crystal. This secular equation yields three eigenvalues which are associated with sound velocities of three phonon waves propagating in the same direction, and three mutually orthogonal eigenvectors which are the polarizations (displacement direction) of waves.

$$\begin{vmatrix} C_{11}I_1I_1+C_{55}I_3I_3+C_{66}I_2I_2-\rho V^2 & C_{12}I_1I_2+C_{66}I_2I_1 & C_{13}I_1I_3+C_{55}I_3I_1 \\ C_{66}I_1I_2+C_{12}I_2I_1 & C_{66}I_1I_1+C_{22}I_2I_2+C_{44}I_3I_3-\rho V^2 & C_{23}I_2I_3+C_{44}I_3I_2 \\ C_{55}I_1I_3+C_{13}I_3I_1 & C_{44}I_2I_3+C_{23}I_3I_2 & C_{44}I_2I_2+C_{33}I_3I_3+C_{55}I_1I_1-\rho V^2 \end{vmatrix}=0 \tag{82}$$

Four phonon propagation directions are discussed below:

(i) Phonon wave propagating along [100] direction ($\vec{q}$//[100]), i.e. I_1=1, I_2=I_3=0, then Eq. (82) becomes

$$\begin{vmatrix} C_{11}-\rho V^2 & 0 & 0 \\ 0 & C_{66}-\rho V^2 & 0 \\ 0 & 0 & C_{55}-\rho V^2 \end{vmatrix}=0 \tag{83}$$

The roots of this equation, i.e. the corresponding values of ρV^2, areC_{11}, C_{66} and C_{55}. The unit eigenvector $\bar{u}=(u_1,u_2,u_3)$ for the eigenvalue $\rho V^2=C_{11}$ can be obtain by

$$\begin{pmatrix} 0 & 0 & 0 \\ 0 & C_{66}-\rho V^2 & 0 \\ 0 & 0 & C_{55}-\rho V^2 \end{pmatrix}\begin{pmatrix} u_1 \\ u_2 \\ u_3 \end{pmatrix}=\begin{pmatrix} 0 \\ 0 \\ 0 \end{pmatrix}=0 \tag{84}$$

Thus

$$\begin{pmatrix} u_1 \\ u_2 \\ u_3 \end{pmatrix}=\begin{pmatrix} 1 \\ 0 \\ 0 \end{pmatrix}$$

Similarly for $\rho V^2=C_{66}$ and $\rho V^2=C_{55}$, the polarization vectors are

$$\begin{pmatrix} u_1 \\ u_2 \\ u_3 \end{pmatrix} = \begin{pmatrix} 0 \\ 1 \\ 0 \end{pmatrix} \qquad \text{for } \rho V^2 = C_{66}$$

$$\begin{pmatrix} u_1 \\ u_2 \\ u_3 \end{pmatrix} = \begin{pmatrix} 0 \\ 0 \\ 1 \end{pmatrix} \qquad \text{for } \rho V^2 = C_{55}$$

Finally, we have

$\rho V_L^2 = C_{11}$	$\vec{n}_L = (1,0,0)$	longitudinal (LA) mode
$\rho V_{T1}^2 = C_{66}$	$\vec{n}_{T1} = (0,1,0)$	transverse (TA) mode
$\rho V_{T2}^2 = C_{55}$	$\vec{n}_{T2} = (0,0,1)$	transverse (TA) mode

The orientations of the phonon propagation wave vector and the three wave polarizations are given in Fig. 26.

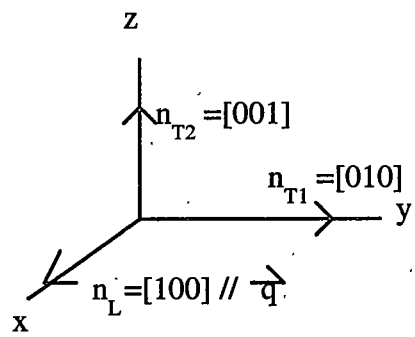

Figure 26. Orientations of phonon propagation wave vector $\vec{q}$ / /[100]and three wave polarizations.

(ii) Phonon propagating along [001] direction ($\vec{q}$//[001]), i.e. I_3=1, I_1=I_2=0. Then Eq. (82) becomes

$$\begin{vmatrix} C_{55}-\rho V^2 & 0 & 0 \\ 0 & C_{44}-\rho V^2 & 0 \\ 0 & 0 & C_{33}-\rho V^2 \end{vmatrix}=0 \qquad (85)$$

The eigenvalues ρV^2 of this equation and the corresponding eigenvectors are

$\rho V_L^2 = C_{33}$	$\vec{n}_L = (0,0,1)$	longitudinal (LA) mode
$\rho V_{T1}^2 = C_{44}$	$\vec{n}_{T1} = (0,1,0)$	transverse (TA) mode
$\rho V_{T2}^2 = C_{55}$	$\vec{n}_{T2} = (1,0,0)$	transverse (TA) mode

(iii) Phonon propagating along [110] direction ($\vec{q}$//[110]), i.e. $I_1=I_2=\sqrt{\frac{1}{2}}$, $I_3=0$.

Then Eq. (82) becomes

$$\begin{vmatrix} \frac{1}{2}(C_{11}+C_{66})-\rho V^2 & \frac{1}{2}(C_{12}+C_{66}) & 0 \\ \frac{1}{2}(C_{66}+C_{12}) & \frac{1}{2}(C_{66}+C_{22})-\rho V^2 & 0 \\ 0 & 0 & \frac{1}{2}(C_{55}+C_{44})-\rho V^2 \end{vmatrix}=0 \qquad (86)$$

$$[(C_{11}+C_{66}-2\rho V^2)(C_{66}+C_{22}-2\rho V^2)-(C_{12}+C_{66})^2](C_{55}+C_{44}-2\rho V^2)=0 \qquad (87)$$

In case of tetragonal symmetry with classes 4mm, $\bar{4}2m$, 422, 4/mmm, one can use the following further symmetry relations

$$C_{11}=C_{22}, \qquad C_{13}=C_{23}, \qquad C_{44}=C_{55}$$

Thus Eq. (87) becomes